

On the Migrating Speed of Free Alternate Bars

Ishihara Michihide¹ and Hiroyasu Yasuda²

¹Hokkaido University

²Research Institute for Natural Hazards & Disaster Recovery Niigata University

November 22, 2022

Abstract

* The spatial distribution of the migrating speed of the free alternate bars that occur in rivers was determined. * The spatial distribution of the migrating speed M of bars was discovered. The formula of M was proposed and its applicability was showed. * The main dominant physical quantity of the migrating speed of alternate bars was found to be the energy slope.

On the Migrating Speed of Free Alternate Bars

Michihide Ishihara¹ and Hiroyasu Yasuda²

¹Graduate School of Engineering, Hokkaido University, Hokkaido, Japan

²Research Institute for Natural Hazards & Disaster Recovery Niigata University, Niigata, Japan

Key Points:

- The spatial distribution of the migrating speed of the free alternate bars that occur in rivers was determined.
- The spatial distribution of the migrating speed M of bars was discovered. The formula of M was proposed and its applicability was showed.
- The main dominant physical quantity of the migrating speed of alternate bars was found to be the energy slope.

Corresponding author: Hiroyasu Yasuda, hiro@gs.niigata-u.ac.jp

Abstract

It has been noted that free alternate bars exhibit wave properties. However, these wave properties, such as the migration speed and spatial distribution, have often been unknown. In this study, we discovered the existence of a migration speed M for free alternate bars, quantified the magnitude of M and its spatial distribution, and further identified the dominant variable of M . Subsequently, we conducted a flume experiment with continuously flowing water and showed the existence of M on measurements of the bed deformation. Moreover, to quantify the spatial distribution of M using the advection velocity of a hyperbolic partial differential equation (HPDE), we assumed that the bottom surface is a continuous function and derived an HPDE for the bed level. Then, to verify the HPDE, we showed that it adequately describes the temporal variation in the bed level. We found that the proposed formula of M can calculate the spatial distribution and the temporally varying of M and in flume experiments. The proposed formula showed that the magnitude of M is 10^{-3} to 10^{-4} orders of magnitude less than the velocity of the uniform flow. We suggested that the dominant physical variables of M are the energy slope, grain size, and Shields number. Afterward, we showed that M obtained from the proposed formula is in agreement with those obtained from an instability analysis. Furthermore, we showed that the proposed formula is applicable to actual rivers, in which the scale and conditions differ from those in experiments.

Plain language summary

Periodic undulating shapes are spontaneously formed in the rivers whose beds are composed of sediments. Such shapes are called riverbed waves because of their geometry and physical properties. Sandbars, which are mesoscale among riverbed waves, are formed on the bottom of the rivers located in alluvial plains. The physical conditions under which sandbars occur and their geometry have been elucidated, and sandbars have been noted to exhibit wave properties. However, these wave properties, which include the migrating speed and spatial distribution, have often been unknown. In this study, we aimed to discover the migration speed of sandbars. We also showed that the migration speed can be quantified by the advection velocity of the partial differential equation of the bottom surface. Furthermore, we showed that the migrating speed in real rivers can be accurately estimated using the derived equations. Based on the results of this study, the behaviors of sandbars in real rivers can be predicted, scientific decisions regarding each of the methods can be made, and countermeasures can be timed. Besides, Riverbed waves seem to be one of self organization phenomenon, the derived advection-diffusion equation will be applied to the elucidation of self organization phenomena.

1 Introduction

Periodic undulating shapes are spontaneously formed in the rivers and streams whose beds are composed of sediments that can be transported by flowing water. Such shapes are called riverbed waves because of their geometry and physical properties. Riverbed waves are classified into small-scale, mesoscale, and mega-scale, depending on the spatial scales, which include the wavelength and wave height (Seminarara, 2010). Small-scale riverbed waves have wavelengths on the scale of the flowing depth, whereas mesoscale riverbed waves have wavelengths on the river width scale and wave heights on the flowing depth scale. As for mega-scale riverbed waves, they have a larger meaning. In this study, we mainly focused on the bars corresponding to mesoscale riverbed waves. Such riverbed waves are often located in alluvial fans and can be broadly classified into two categories: 1) free alternate bars, which occur spontaneously in straight channels owing to the instability of the bottom sur-

62 face; and 2) forced bars, which occur because of steady forces, such as meanders or
63 gryones (Seminara, 2010). When observing a unique periodic geometry of free al-
64 ternate bars from the sky using aerial photographs (Figure 1(a)), the shape of the
65 streams at low flow rates is reflected by left banks or right banks, similar to the
66 waveguide phenomenon, and deep-water pools are placed downstream of the points
67 where streams are turned around. The geometry of free alternate bars is shifted
68 during floods, especially when sediment transport is active, similar to water sur-
69 face waves (Figure 1(a),(b)). Over the years, various physical properties of free al-
70 ternate bars have been studied. Through long-term flume experiments, Kinoshita
71 (1961) investigated the change from flat beds to alternate bars and its development
72 processes, which can produce meandering streams. Moreover, he reported that 1)
73 alternate bars have a globally uniform migrating speed and wavelength and that 2)
74 they have short wavelengths and fast migrating speeds in the early stages of devel-
75 opment. 3) He also reported that the migrating speed decreases with the increase in
76 the wavelength. These results have been confirmed in subsequent studies (Fujita &
77 Muramoto, 1982; Ikeda, 1983; Fujita & Muramoto, 1985; Nagata et al., 1999). More-
78 over, Kinoshita proposed a formula for calculating the migrating speed of alternate
79 bars based on his experimental results in the above study. However, the validity of
80 the formula has not been demonstrated yet.

81 Callander (1969) extended the instability analysis proposed by Kennedy (1963)
82 for small-scale riverbed waves to a two-dimensional plane problem in which alter-
83 nate bars occur. In addition, in the same study, it was indicated that the instability
84 of movable bed surfaces is related to the channel width. Kennedy's study led to a
85 unified study on the occurrence mechanism of small-scale and mesoscale riverbed
86 waves using an instability analysis with a phase lag distance (Hayashi et al., 1982;
87 Ozaki & Hayashi, 1983). Moreover, several studies have been conducted to predict
88 the occurrence conditions of alternate bars and their geometries as wavelength and
89 wave height during their development (Kuroki & Kishi, 1984; Colombini et al., 1987;
90 Colombini & Tubino, 1991; Tubino, 1991; Schielen et al., 1993; Izumi & Pornprom-
91 min, 2002; Bertagni et al., 2018). These studies, which employed instability analyses,
92 also provided formulas for calculating the migrating speeds of the bed perturbations
93 at the wavenumbers of the maximum amplification rates. However, these formulas
94 only allow the calculation of the migrating speeds of specific wavenumbers and not
95 the spatial distributions of migrating speeds.

96 Shimizu and Itakura (1989) developed a numerical simulation for reproducing
97 the transformation of flat beds into alternate bars and its development processes,
98 and they reported that a simulation can satisfactorily reproduce these processes.
99 Currently, one of the primary research methods is numerical analysis. In many pre-
100 vious studies employing numerical analyses, the reproducibility of the geometry of
101 bars during occurrence and development was mainly discussed. However, neither the
102 temporal variation of the migrating speed nor its spatial distribution was discussed.
103 A related study is the study of the migration direction of bed perturbations perform-
104 ing instability and numerical analyses by Federici and Seminara (2003).

105 The effects of external factors, such as the amount of sediment supply and flow
106 discharge, on the deformation of alternate bars have been investigated using labo-
107 ratory flume experiments (Lanzoni, 2000a, 2000b; Miwa et al., 2007; Crosato et al.,
108 2011, 2012; Venditti et al., 2012; Podolak & Wilcock, 2013). Crosato et al. (2011,
109 2012) reported that alternate bars eventually shift from being migrating bars to
110 steady bars. Then, to verify this conclusion, they further performed flume experi-
111 ments and a numerical analysis. Venditti et al. (2012) reported that when the sedi-
112 ment supply is interrupted after the occurrence and development of alternate bars,
113 the bed slope and Shields number decrease, and the bars accordingly disappear.
114 Podolak and Wilcock (2013) studied the response of alternate bars to the supply

115 of sediments by increasing the sediment supply during the occurrence and develop-
116 ment of alternate bars. He then reported that nonmigrating bars are transformed
117 into migrating bars with the increase in the bed slope and Shields number due to
118 the increase in the sediment supply, and this conclusion was further investigated in a
119 subsequent study (Nelson & Morgan, 2018).

120 The deformation processes of alternate bars in actual rivers were investigated
121 in (Eekhout et al., 2013; Adami et al., 2016). Eekhout et al. (2013) measured the
122 geometry of alternate bars in rivers for nearly three years and reported that the mi-
123 grating speed decreases with the increase in the wavelength and wave height of al-
124 ternate bars and the decrease in the bed slope. Adami et al. (2016) studied the be-
125 havior of alternate bars in the Alps and Rhine River over several decades, and they
126 established a relationship between the flow discharge and migrating speed of bars.
127 In addition, they confirmed that bars move less when the flow rate is very high and
128 that they move frequently when the flow discharge is in the middle scale of the flow
129 discharge.

130 The above studies indicate that free alternate bars have wave properties. How-
131 ever, the details of these wave properties and a formula for estimating the migrating
132 speed of free alternate bars have not yet been established. In this study, aiming at
133 understanding the wave properties of alternate bars, we proved the existence of spa-
134 tial distribution for the migrating speeds of alternate bars and proposed a formula
135 for estimating migrating speeds. In §2, an outline of the laboratory flume experi-
136 ment and the measurement results are described. In §3, to quantify the spatial dis-
137 tribution of the migrating speed of alternate bars using the coefficient (advection
138 velocity) of the advection term in a HPDE, we assumed that the bed level is a con-
139 tinuous function and derived an HPDE for the bed level. We used this coefficient as
140 a formula for calculating the migrating speed. In §4, to verify the HPDE, we showed
141 that it adequately describes the temporal variation at the bed level. The spatial dis-
142 tribution of the migrating speed of alternate bars was also quantified using the de-
143 rived formula. In §5, we showed the dominant physical quantities of the migrating
144 speed and determined the magnitude of the migrating speed of alternate bars. In ad-
145 dition, we showed that the migrating speed obtained from the derived formula is in
146 agreement with those obtained from instability analyses. In §6, the applicability of
147 the proposed formula to real rivers is discussed. Finally, §7 summarizes the research
148 results.

149 **2 Experiments**

150 **2.1 Experimental setup**

151 Figure 2 shows a plane view of the laboratory experimental flume, which is
152 straight and has a rectangular cross section. Moreover, it has a length of 12.0 m, a
153 width of 0.45 m, and a depth of 0.15 m. 6 m of the total length of this flume were
154 filled with a 5-cm-thick layer of 0.76-mm grain sand to create a section of the mov-
155 ing bed. For the steady supply of water to the channel, circulation-type pumping
156 from a water tank at the downstream end to a water tank at the upstream end was
157 used, and the accuracy of the water discharge was confirmed using an electromag-
158 netic flowmeter.

159 **2.2 Experimental conditions**

160 In this study, we aimed at obtaining the spatial distribution of the migrating
161 speed of free alternate bars and at determining their scale and dominant physical
162 quantities. In the following experiment, we set up the hydraulic conditions under
163 which alternate bars are expected to develop and migrate. It has been theoretic-

164 cally shown that the occurrence of alternate bars can be estimated using the chan-
 165 nel width B / depth h_0 ratio β (Callander, 1969; Kuroki & Kishi, 1984). Kuroki
 166 and Kishi (1984) showed that the types of occurring bars can be classified based on
 167 $BI_0^{0.2}/h_0$, which is the bed slope I_0 added to the channel width/depth ratio. In this
 168 study, we set two conditions that correspond to the region of occurrence of alternate
 169 bars, as shown in Table 1.

Table 1. Experimental conditions.

Case	Flow discharge [L/s]	width [m]	slope	h_0 [m]	$BI_0^{0.2}/h_0$	β	τ_*
1	2.0	0.45	1/160	0.014	11.4	16.07	0.0713
2	2.6	0.45	1/200	0.018	8.7	12.50	0.0714

170 These experimental conditions exceed the critical Shields number of 0.034,
 171 which can be obtained from the equation of Iwagaki (1956). The sediment feed con-
 172 dition at the upstream end was set to no feed. In preparation for this study, we
 173 examined the spatial distribution of migrating speeds under different sand feeding
 174 conditions and confirmed that the spatial distribution of migrating speeds is clearer
 175 without sand feeding than with sand feeding. The same experiment was conducted
 176 twice for each condition to confirm the reproducibility of the results.

177 2.3 Measurement method for the bed surface and water surface

178 In most of the previous studies using flume experiments, the temporal changes
 179 of the bars' geometry in the development process were not measured in a single con-
 180 tinuous experiment, and the changes in the flowing depth associated with the de-
 181 velopment process were not estimated. In this study, in a single continuous experi-
 182 ment, we measured the bed and water levels in a plane while the water was flowing
 183 using stream tomography (ST) (Moteki et al., 2022). The flowing depth could also
 184 be obtained from the measurements using ST, and this flowing depth is given in the
 185 formula of the migrating speed, which is discussed in §3. We measured the bed and
 186 water levels with a spatial resolution of 2 cm² for every minute. There were no mea-
 187 surements near the sidewalls due to ST limitations. Thus, data for a width of 0.38
 188 m, excluding the places near sidewalls, were used in this study.

189 2.4 Measurement results

190 We described the migration phenomena of free alternate bars based on high-
 191 resolution spatial measurements by ST, where we used a plane view of the bed level,
 192 as shown in Figure 3, and a longitudinal section, as shown in Figure 4. The fig-
 193 ures show the measurement results of case 2, where typical free alternate bars were
 194 formed. The measurement results for the other conditions only differ from those
 195 of case 2 with regard to the wavelength and wave height; there is no essential dif-
 196 ference. For the measurement results of the other conditions, please refer to the
 197 database (Ishihara & Yasuda, 2022).

198 Figure 3 shows a plane view of the deviation of the bed level. The origin of the
 199 vertical coordinates of the measurement is the bottom of the flume, and the water
 200 and bed level show the height from the bed of the flume. In this study, the initial
 201 bed was formed as flat in the transverse direction as possible. However, a flatbed
 202 could not be realized due to the limitation of the molding attachment. It can be
 203 inferred that the transverse slope of the initial bed had some effects on the devel-

204 opment of the bars. However, the above-measured temporal variation of the bars
 205 corresponds to that of previous studies (Kinoshita, 1958; Federici & Seminara, 2003;
 206 Crosato et al., 2011; Venditti et al., 2012; Podolak & Wilcock, 2013). We also found
 207 that the measured results are compatible with the instability analysis discussed in §5
 208 below. The measured wavelength and wave height of the bars at the final time of the
 209 experiment shown in Figure 3 were approximately 0.01 m and 1.4 m, respectively.
 210 The equilibrium wave heights and wavelengths obtained from the instability analy-
 211 sis are 0.0097 m and 1.42 m. These results suggest that the transverse slope of the
 212 initial bed is not a concern.

213 Figure 3 from (a) to (d) shows that the bottom shape did not change much
 214 from the initial flat bed. Figure 3(e) shows that an alternating deposition and a
 215 scour were formed in the downstream section, indicating the occurrence of bars.
 216 Since the geometrical features of the alternate bars were first recognized in this fig-
 217 ure, in this study, this time was defined as the occurrence time of the bars. After
 218 that, the measured bars showed more deposition in the deposited areas and more
 219 scours in the scoured areas, which is a typical temporal development. All the bars
 220 were gradually migrating downstream at that time. In the series of observations
 221 from Figure 3(g) 60 min to Figure 3(m) 120 min, the bar was migrating at a con-
 222 stant speed.

223 Figure 4 shows the longitudinal distribution of the deviation in the bed level
 224 on the green dotted line in Figure 3. Figure 4 shows (a) the initial stage of the ex-
 225 periment, (b) the occurrence of alternate bars, (c) the intermediate stage of the ex-
 226 periment, and (d) the final stage of the experiment. Figure 4 shows three results 10
 227 min apart, and Figure 4(a) shows that the deviation of the bed level was almost flat
 228 from 1 to 20 minutes. Figure 4(a) shows that three bed undulations were formed
 229 at 2.5 m, 4.5 m, and 5.5 m from the upstream end after 60 min from the beginning
 230 of the experiment. Then, the amplitudes of their bed undulations were developed,
 231 and they migrated in the downstream direction. From Figure 4(b) 60 to 120 min,
 232 this undulation migrated downstream with an increasing wave height. These results
 233 indicate that the wave property of the bars could be measured. As shown in Fig-
 234 ure 4(d), a decrease in the bed level can be observed in the upstream section. How-
 235 ever, this is because the experimental conditions were set without a sediment supply.
 236 Nevertheless, there was no decrease in the bed level at downstream half the channel,
 237 even at the end of the experiment. This suggests that the effect of the no-sediment
 238 supply condition did not spread downstream of half the channel at the end of the
 239 experiment.

240 The linear wave theory indicates that a phase propagates without waveform
 241 deformation if a wave propagates with a spatial, temporal, and constant migrating
 242 speed. Conversely, based on the nonlinear wave theory, in which the migrating speed
 243 has spatial distribution and temporal changes, a wave propagates with waveform de-
 244 formation. From the viewpoint of the above wave theories, the migrating speed of
 245 the bars after the occurrence of alternate bars in Figure 4(b) has spatial distribu-
 246 tion and is estimated to change with time. Moreover, it has the characteristics of a
 247 nonlinear wave.

248 3 2-D Model formulation

249 As shown in the previous section, the measurement results of this study show
 250 the wave properties of free alternate bars during their occurrence and development.
 251 These results are mostly consistent with those of previous studies (Kinoshita, 1958;
 252 Federici & Seminara, 2003; Crosato et al., 2011; Venditti et al., 2012; Podolak &
 253 Wilcock, 2013).

254 The wave phenomena generally describe the wave equation by an HPDE, and
 255 the phase speed of wave is described coefficient (advection velocity) of the advection
 256 term in the equation. The wave equation for water surface waves was derived by as-
 257 suming that the water surface is a continuous function. If the bed surface is assumed
 258 to be a continuous function, the wave equation for the bed surface can be derived,
 259 and the coefficients of the advection term in the equation can be applied to calcu-
 260 late the migrating speed of the bars and its spatial distribution. Indeed, this type
 261 of equation has been previously derived (Fujita et al., 1985). However, its applica-
 262 bility has rarely been investigated. Also, in instability analyses, the migrating speed
 263 can be quantified (Callander, 1969; Kuroki & Kishi, 1984). However, the quantify of
 264 the speed in instability analyses, only the migrating speed for each wavenumber is
 265 estimated, and the spatial distribution of the migrating speed cannot be quantified.
 266 As mentioned above, a method for quantifying the migrating speed and its spatial
 267 distribution has not yet been established.

268 We derived an HPDE for the bed level to quantify the migrating speed. The
 269 equation of the bed level has a total of four different forms: steady or unsteady for
 270 the description of time and one-dimensional or two-dimensional for the description
 271 of space. We showed that the magnitude of unsteady in the physics of this study
 272 is negligible, as described in Appendix A. Regarding the time description, we only
 273 used the steady form. In the following derivations, we show the derivation of the
 274 steady form. The geometries of the alternate bars and the flow therein have a two-
 275 dimensional characteristic. As for the space description, we only treated the two-
 276 dimensional form. In the following derivations, we show the derivation of the two-
 277 dimensional form.

278 The equation for the bed level z was derived by coupling three equations: the
 279 continuity equation of the sediment, the sediment function, and the equation of the
 280 water surface profile. For the derivation of the HPDE, the Exner equation, as the
 281 continuous equation of the sediment, only included the Meyer–Peter and Müller
 282 (MPM) formula as the sediment function and the two-dimensional equation of the
 283 water surface profile, respectively. In this study, MPM was adopted because 1) the
 284 simplified form of the MPM enables plain mathematical operations. Moreover, 2)
 285 we confirmed that MPM can describe the physics of this study, as described in §4.
 286 To describe the sediment flux in planar two dimensions, we used the equations for
 287 each directional component derived by Watanabe et al. (2001), as shown in Eq. (2)
 288 and Eq. (3). The Shields number calculate Equation (7). To derive an HPDE for
 289 the bed level, we newly derived the steady two-dimensional equation of the water
 290 surface profile of Eq. (5) and Eq. (6). For details on the derivation of the steady
 291 two-dimensional equation for the water surface profile, please refer to Appendix B.

$$\frac{\partial z}{\partial t} + \frac{1}{1-\lambda} \left(\frac{\partial q_{Bx}}{\partial x} + \frac{\partial q_{By}}{\partial y} \right) = 0 \quad (1)$$

292

$$q_{Bx} = 8 (\tau_* - \tau_{*c})^{3/2} \sqrt{sgd^3} \left(\frac{u}{V} - \frac{\gamma'}{\tau_*^{1/2}} \frac{\partial z}{\partial x} \right) \quad (2)$$

293

$$q_{By} = 8 (\tau_* - \tau_{*c})^{3/2} \sqrt{sgd^3} \left(\frac{v}{V} - \frac{\gamma'}{\tau_*^{1/2}} \frac{\partial z}{\partial y} \right) \quad (3)$$

294

$$\gamma' = \sqrt{\frac{\tau_{*c}}{\mu_s \mu_k}} \quad (4)$$

295

$$\frac{\partial h}{\partial x} = -\frac{\partial z}{\partial x} - I_{ex} - \frac{3}{5} \frac{u^2}{gI_{ex}} \frac{\partial I_{ex}}{\partial x} + \frac{3}{10} \frac{u^2}{gI_e} \frac{\partial I_e}{\partial x} + \frac{2}{5} \frac{uv}{gI_{ey}} \frac{\partial I_{ey}}{\partial y} + \frac{3}{10} \frac{uv}{gI_e} \frac{\partial I_e}{\partial y} - \frac{uv}{gI_{ex}} \frac{\partial I_{ex}}{\partial y} \quad (5)$$

296

$$\frac{\partial h}{\partial y} = -\frac{\partial z}{\partial y} - I_{ey} - \frac{3}{5} \frac{v^2}{gI_{ey}} \frac{\partial I_{ey}}{\partial y} + \frac{3}{10} \frac{v^2}{gI_e} \frac{\partial I_e}{\partial y} + \frac{2}{5} \frac{uv}{gI_{ex}} \frac{\partial I_{ex}}{\partial x} + \frac{3}{10} \frac{uv}{gI_e} \frac{\partial I_e}{\partial x} - \frac{uv}{gI_{ey}} \frac{\partial I_{ey}}{\partial x} \quad (6)$$

297

$$\tau_* = \frac{hI_e}{sd} \quad (7)$$

298

299

300

301

302

303

304

305

306

307

where z is the bed level, t is the time, λ is the porosity of the bed, q_{Bx} is the longitudinal sediment flux, x is the distance of the longitudinal direction, q_{By} is the transverse sediment flux, y is the distance of the transverse direction, τ_* is the composite Shields number, τ_{*c} is the critical Shields number, s is the specific gravity of the sediments in water, g is the acceleration due to gravity, d is the sediment size, u is the longitudinal flow velocity, V is the composite flow velocity, v is the transverse flow velocity, μ_s is the coefficient of static friction, μ_k is the coefficient of dynamic friction, and h is the depth. In addition, $I_{bx} = -\partial z/\partial x$ is the longitudinal bed slope, I_{ex} is the longitudinal energy slope, $I_{by} = -\partial z/\partial y$ is the transverse bed slope, and I_{ey} is the transverse energy slope.

308

To obtain $\partial q_{Bx}/\partial x$ in Eq. (1), the chain rule of differentiation was applied.

$$\begin{aligned} \frac{\partial q_{Bx}}{\partial x} &= \frac{\partial q_{Bx}}{\partial \tau_*} \frac{\partial \tau_*}{\partial x} + \frac{\partial q_{Bx}}{\partial u} \frac{\partial u}{\partial x} + \frac{\partial q_{Bx}}{\partial V} \frac{\partial V}{\partial x} + \frac{\partial q_{Bx}}{\partial (\partial z/\partial x)} \frac{\partial (\partial z/\partial x)}{\partial x} \\ &= \frac{\partial q_{Bx}}{\partial \tau_*} \left(\frac{\partial \tau_*}{\partial h} \frac{\partial h}{\partial x} + \frac{\partial \tau_*}{\partial I_e} \frac{\partial I_e}{\partial x} \right) + \frac{\partial q_{Bx}}{\partial u} \frac{\partial u}{\partial x} + \frac{\partial q_{Bx}}{\partial V} \frac{\partial V}{\partial x} + \frac{\partial q_{Bx}}{\partial (\partial z/\partial x)} \frac{\partial^2 z}{\partial x^2} \\ &= \frac{\partial q_{Bx}}{\partial \tau_*} \left(\frac{I_e}{sd} \frac{\partial h}{\partial x} + \frac{h}{sd} \frac{\partial I_e}{\partial x} \right) + \frac{\partial q_{Bx}}{\partial u} \frac{\partial u}{\partial x} + \frac{\partial q_{Bx}}{\partial V} \frac{\partial V}{\partial x} + \frac{\partial q_{Bx}}{\partial (\partial z/\partial x)} \frac{\partial^2 z}{\partial x^2} \\ &= \frac{\partial q_{Bx}}{\partial \tau_*} \frac{I_e}{sd} \left(\frac{\partial h}{\partial x} + \frac{h}{I_e} \frac{\partial I_e}{\partial x} \right) + \frac{\partial q_{Bx}}{\partial u} \frac{\partial u}{\partial x} + \frac{\partial q_{Bx}}{\partial V} \frac{\partial V}{\partial x} + \frac{\partial q_{Bx}}{\partial (\partial z/\partial x)} \frac{\partial^2 z}{\partial x^2} \end{aligned} \quad (8)$$

309

where n is the roughness coefficient.

310

311

When the chain rule of differentiation and Manning's velocity formula of the uniform flow Eq. (9) as below, $\partial I_e/\partial x$ in Eq. (8) can be obtained.

$$V = \frac{1}{n} I_e^{1/2} h^{2/3} \quad (9)$$

312

$$\frac{\partial I_e}{\partial x} = \frac{\partial I_e}{\partial h} \frac{\partial h}{\partial x} + \frac{\partial I_e}{\partial V} \frac{\partial V}{\partial x} = -\frac{4}{3} \frac{I_e}{h} \frac{\partial h}{\partial x} + 2 \frac{I_e}{V} \frac{\partial V}{\partial x} \quad (10)$$

313

Eq. (10) in Eq. (8) and rearranging, the following equation could be obtained.

$$\frac{\partial q_{Bx}}{\partial x} = \frac{\partial q_{Bx}}{\partial \tau_*} \frac{I_e}{sd} \left(-\frac{1}{3} \frac{\partial h}{\partial x} + 2 \frac{h}{V} \frac{\partial V}{\partial x} \right) + \frac{\partial q_{Bx}}{\partial u} \frac{\partial u}{\partial x} + \frac{\partial q_{Bx}}{\partial V} \frac{\partial V}{\partial x} + \frac{\partial q_{Bx}}{\partial (\partial z/\partial x)} \frac{\partial^2 z}{\partial x^2} \quad (11)$$

314

315

$\partial q_{Bx}/\partial \tau_*$, $\partial q_{Bx}/\partial u$, $\partial q_{Bx}/\partial V$, and $\partial q_{Bx}/\partial (\partial z/\partial x)$ in the above equation are as follows.

$$\frac{\partial q_{Bx}}{\partial \tau_*} = 8 (\tau_* - \tau_{*c})^{1/2} \sqrt{sgd^3} \frac{3}{2} \left[\frac{u}{V} - \frac{\gamma'}{\tau_*^{1/2}} \left\{ 1 - \frac{1}{3\tau_*} (\tau_* - \tau_{*c}) \right\} \frac{\partial z}{\partial x} \right] \quad (12)$$

316

$$\frac{\partial q_{Bx}}{\partial u} = 8 (\tau_* - \tau_{*c})^{3/2} \sqrt{sgd^3} \frac{1}{V} \quad (13)$$

317

$$\frac{\partial q_{Bx}}{\partial V} = -8 (\tau_* - \tau_{*c})^{3/2} \sqrt{sgd^3} \frac{u}{V^2} \quad (14)$$

318

$$\frac{\partial q_{Bx}}{\partial(\partial z/\partial x)} = -8 (\tau_* - \tau_{*c})^{3/2} \sqrt{sgd^3} \frac{\gamma'}{\tau_*^{1/2}} \quad (15)$$

319 Equation (5) was used for $\partial h/\partial x$. Eq. (5), Eq. (12), Eq. (13), Eq. (14), and Eq.
320 (15) in Eq. (11). Eq. (11) becomes as follows.

$$\begin{aligned} & \frac{\partial q_{Bx}}{\partial x} = 4 (\tau_* - \tau_{*c})^{1/2} \sqrt{sgd^3} \frac{I_e}{sd} \left[\frac{u}{V} - \frac{\gamma'}{\tau_*^{1/2}} \left\{ 1 - \frac{1}{3\tau_*} (\tau_* - \tau_{*c}) \right\} \frac{\partial z}{\partial x} \right] \\ & \left\{ \frac{\partial z}{\partial x} + I_{ex} + \frac{3}{5} \frac{u^2}{gI_{ex}} \frac{\partial I_{ex}}{\partial x} - \frac{3}{10} \frac{u^2}{gI_e} \frac{\partial I_e}{\partial x} - \frac{2}{5} \frac{uv}{gI_{ey}} \frac{\partial I_{ey}}{\partial y} - \frac{3}{10} \frac{uv}{gI_e} \frac{\partial I_e}{\partial y} + \frac{uv}{gI_{ex}} \frac{\partial I_{ex}}{\partial y} + 6 \frac{h}{V} \frac{\partial V}{\partial x} \right\} \\ & + 8 (\tau_* - \tau_{*c})^{3/2} \sqrt{sgd^3} \frac{1}{V} \frac{\partial u}{\partial x} - 8 (\tau_* - \tau_{*c})^{3/2} \sqrt{sgd^3} \frac{u}{V^2} \frac{\partial V}{\partial x} - 8 (\tau_* - \tau_{*c})^{3/2} \sqrt{sgd^3} \frac{\gamma'}{\tau_*^{1/2}} \frac{\partial^2 z}{\partial x^2} \end{aligned} \quad (16)$$

321 $\partial q_{By}/\partial y$ was arranged in the same process as Eq. (16), and the following equation
322 could be obtained.

$$\begin{aligned} & \frac{\partial q_{By}}{\partial y} = 4 (\tau_* - \tau_{*c})^{1/2} \sqrt{sgd^3} \frac{I_e}{sd} \left[\frac{v}{V} - \frac{\gamma'}{\tau_*^{1/2}} \left\{ 1 - \frac{1}{3\tau_*} (\tau_* - \tau_{*c}) \right\} \frac{\partial z}{\partial y} \right] \\ & \left\{ \frac{\partial z}{\partial y} + I_{ey} + \frac{3}{5} \frac{v^2}{gI_{ey}} \frac{\partial I_{ey}}{\partial y} - \frac{3}{10} \frac{v^2}{gI_e} \frac{\partial I_e}{\partial y} - \frac{2}{5} \frac{uv}{gI_{ex}} \frac{\partial I_{ex}}{\partial x} - \frac{3}{10} \frac{uv}{gI_e} \frac{\partial I_e}{\partial x} + \frac{uv}{gI_{ey}} \frac{\partial I_{ey}}{\partial y} + 6 \frac{h}{V} \frac{\partial V}{\partial y} \right\} \\ & + 8 (\tau_* - \tau_{*c})^{3/2} \sqrt{sgd^3} \frac{1}{V} \frac{\partial v}{\partial y} - 8 (\tau_* - \tau_{*c})^{3/2} \sqrt{sgd^3} \frac{v}{V^2} \frac{\partial V}{\partial y} - 8 (\tau_* - \tau_{*c})^{3/2} \sqrt{sgd^3} \frac{\gamma'}{\tau_*^{1/2}} \frac{\partial^2 z}{\partial y^2} \end{aligned} \quad (17)$$

323 Eq. (16) and Eq. (17) in Eq. (1), the following HPDE for the bed level z could be
324 derived. This equation is classified as an advection–diffusion equation because it in-
325 cludes a diffusion term.

$$\frac{\partial z}{\partial t} + M_x \frac{\partial z}{\partial x} + M_y \frac{\partial z}{\partial y} = D \frac{\partial^2 z}{\partial x^2} + D \frac{\partial^2 z}{\partial y^2} - M_x (I_{ex} + F_x) - M_y (I_{ey} + F_y) - F_{x2} - F_{y2} \quad (18)$$

326 In the above equation, M_x is the advection velocity of the longitudinal component
327 of the bed level z , and it is assumed to be closely related to the migrating speed of
328 the longitudinal component of alternate bars, which is the subject of this study. M_y
329 is the transverse migrating speed of the alternate bars. M_x and M_y are not the ve-
330 locities of the sediments and are supposed to denote the migrating speeds of the bed
331 level z . M_x and M_y are given as follows.

$$M_x = \frac{4 (\tau_* - \tau_{*c})^{1/2} \sqrt{sgd^3} I_e}{sd(1-\lambda)} \left[\frac{u}{V} - \frac{\gamma'}{\tau_*^{1/2}} \left\{ 1 - \frac{1}{3\tau_*} (\tau_* - \tau_{*c}) \right\} \frac{\partial z}{\partial x} \right] \quad (19)$$

332

$$M_y = \frac{4 (\tau_* - \tau_{*c})^{1/2} \sqrt{sgd^3} I_e}{sd(1-\lambda)} \left[\frac{v}{V} - \frac{\gamma'}{\tau_*^{1/2}} \left\{ 1 - \frac{1}{3\tau_*} (\tau_* - \tau_{*c}) \right\} \frac{\partial z}{\partial y} \right] \quad (20)$$

333 Eq. (19) and Eq. (20) indicate that the dominant physical quantities of the migrat-
334 ing speed are I_e , τ_* , and d . The diffusion coefficient D , F_x , F_y , F_{x2} , and F_{y2} are
335 given as follows.

$$D = \frac{8 (\tau_* - \tau_{*c})^{3/2} \sqrt{sgd^3} \gamma'}{1-\lambda} \frac{\gamma'}{\tau_*^{1/2}} \quad (21)$$

336

$$F_x = \frac{3}{5} \frac{u^2}{gI_{ex}} \frac{\partial I_{ex}}{\partial x} - \frac{3}{10} \frac{u^2}{gI_e} \frac{\partial I_e}{\partial x} - \frac{2}{5} \frac{uv}{gI_{ey}} \frac{\partial I_{ey}}{\partial y} - \frac{3}{10} \frac{uv}{gI_e} \frac{\partial I_e}{\partial y} + \frac{uv}{gI_{ex}} \frac{\partial I_{ex}}{\partial y} + 6 \frac{h}{V} \frac{\partial V}{\partial x} \quad (22)$$

337

$$F_y = \frac{3}{5} \frac{v^2}{gI_{ey}} \frac{\partial I_{ey}}{\partial y} - \frac{3}{10} \frac{v^2}{gI_e} \frac{\partial I_e}{\partial y} - \frac{2}{5} \frac{uv}{gI_{ex}} \frac{\partial I_{ex}}{\partial x} - \frac{3}{10} \frac{uv}{gI_e} \frac{\partial I_e}{\partial x} + \frac{uv}{gI_{ey}} \frac{\partial I_{ey}}{\partial x} + 6 \frac{h}{V} \frac{\partial V}{\partial y} \quad (23)$$

338

$$F_{x2} = \frac{8(\tau_* - \tau_{*c})^{3/2} \sqrt{sgd^3}}{1 - \lambda} \left(\frac{1}{V} \frac{\partial u}{\partial x} - \frac{u}{V^2} \frac{\partial V}{\partial x} \right) \quad (24)$$

339

$$F_{y2} = \frac{8(\tau_* - \tau_{*c})^{3/2} \sqrt{sgd^3}}{1 - \lambda} \left(\frac{1}{V} \frac{\partial v}{\partial y} - \frac{v}{V^2} \frac{\partial V}{\partial y} \right) \quad (25)$$

340

4 Application of the proposed model to experiments

341

342

343

344

345

346

347

348

349

350

Measurement methods for the spatial distribution of the migrating speed of alternate bars have not yet been established. One of the methods for quantifying the spatial distribution is the use of a mathematical model. In the previous section, we derived an HPDE for the bed level to quantify the migrating speed. If the HPDE can adequately describe the temporal variation of the bed level, the migrating speed calculated by the coefficient (advection velocity) of the advection term of the HPDE can be assumed to be reasonable. We show that this HPDE can adequately describe the temporal variation in the bed level and then demonstrated that the coefficients can be used in a formula for calculating the spatial distribution of the migrating speed.

351

4.1 Model validation

352

4.1.1 Validation methods

353

354

355

We demonstrated the validity of the temporal variation in the bed level in the HPDE of Eq. (18) by the numerical integration of the HPDE. The time integral of the HPDE can be described by Eq. (26).

$$\Delta z_{\text{cal}} = \left\{ -M_x \frac{\partial z}{\partial x} - M_y \frac{\partial z}{\partial y} + D \frac{\partial^2 z}{\partial x^2} + D \frac{\partial^2 z}{\partial y^2} - M_x (I_{ex} + F_x) - M_y (I_{ey} + F_y) - F_{x2} - F_{y2} \right\} \Delta t \quad (26)$$

356

357

358

359

360

361

362

363

Eq. (26) yields the change amount in the bed level for Δt based on the flowing depth, bed level, flow velocities, and energy slope. We performed this numerical integration using the finite difference method. This integration was performed for each point to obtain the change amount in the bed level, and the results showed the spatial distribution of the change amounts in the bed level. Also, this integration was repeated to obtain a temporal waveform of the variation amount in the bed level at a particular point. This integral was driven through measurements, and it is different from the typical integral driven by the model.

364

4.1.2 Hydraulics required for validation

365

366

367

368

369

As mentioned above, the numerical integration of Eq. (26) must give three quantities: the flowing depth, bed level, the flowing velocity, and the energy slope at the same time. The flowing depth can be obtained from the bed level and the water level measured by ST in §2. However, it is difficult to measure the flowing velocity and energy slope that are paired with the flowing depth. Even ST only measures

the water and bed surface. To determine the flowing velocity paired with the flowing depth measured by ST, we performed numerical analyses.

We employed Nays2D, which is a solver for two-dimensional plane hydraulic analyses and is included in iRIC (Shimizu et al., 2019). The calculation was conducted with a bed level measured by ST as a fixed bed. The spatial directional grid was set as a 2-cm square grid with the same spatial resolution of ST. The boundary condition at the upstream was given the discharge, and the boundary condition at the downstream was given the measured flowing depth in §2. Manning’s roughness coefficients were constant values over the entire analysis domain at each measurement time of the ST. The coefficients at each measurement time were determined by iterative calculations with the coefficients as variables. When the difference between the calculated and measured flowing depths was minimized, a coefficient was determined to be the coefficient at that time.

The measured flowing depths are shown in Figure 5. The difference between the measured and calculated flowing depth Δh_* is shown in Figure 6, and it is nondimensionalized by measurement. The calculated flowing velocities are shown in Figure 7. Of these, Δh_* indicates the computational accuracy of the numerical analysis. Considering Δh_* in Figure 6, Δh_* is generally within 10% for the entire channel at all times regardless of the development of any alternate bars. In the area where the flowing depth was very shallow, Δh_* was greater than 20%. Currently, there are no methods for obtaining the spatial distribution of the flowing velocity paired with the spatial distribution of the flowing depth. For this reason, we decided to use the calculated velocity, as shown below.

4.1.3 Validation results

We showed the validation results of the spatial distribution of the change amount in the bed level and the temporal waveform at a particular point, respectively. We calculated the change amount in the bed level as follows.

$$\Delta z_* = |\Delta z_{\text{obs}} - \Delta z_{\text{cal}}|/d \times 100 \quad (27)$$

where Δz_{obs} is the difference in the bed level at neighboring measurement times in §2, Δz_{cal} is the difference in the bed level at neighboring calculation times based on HPDE, and Δz_* is the difference between Δz_{obs} and Δz_{cal} .

Figure 8 shows plane view of the bed level, and Δz_* . Figure 8 shows the results for 1 min from the beginning of the experiment, where Δz_* was generally less than 100%, and Δz_* was less than the particle size d . Δz_* from Figure 8(b) 10 min to (f) 50 min from the beginning of the experiment, areas exceeding 500% occurred periodically in the longitudinal direction, and their total area accounted for approximately 40%. The bed surface at this time exhibited small irregularities as high as Δz_* . 60 min from the beginning of the experiment, Figure 8(g) shows that the small irregularities of the bed surface disappeared and that distinct bars were formed instead. Moreover, Δz_* became less than 100%. The above results show that the proposed HPDE is at least sufficiently applicable to the stage of distinct bars.

The HPDE was derived based on the assumption that the bed level is a continuous function. Whether a continuous function of the bed level can be obtained from the HPDE can be confirmed by obtaining the temporal waveform at a particular point. The temporal variation in the bed level was obtained by repeating the above numerical integration during each measurement time by ST. The measurements by ST were taken at 1-minute intervals, and the time interval Δt for the numerical integration of Eq. (26) was also set to 1 minute.

6.0 m from the upstream end, Figure 9 shows the temporal variation in the bed level of (a) the left bank side, (b) central part, and (c) right bank side. The red line shows the bed level of the measured value, and the blue line shows the bed level calculated from the integrated HPDE. As shown in Figure 9 (a), (b), and (c), the calculated values after 60 minutes from the beginning of the experiment could well reproduce the measured values. Their integration interval was set to 1 minute, which is much more than the time interval in ordinary numerical analyses. Although the temporal waveform contains high-frequency components, the calculated continuously values could well reproduce the measured values. Thus, the proposed HPDE in this study can adequately describe the temporal variation in bed levels.

4.2 Quantification of the migrating speed of alternate bars

In this subsection, we quantified the spatial distribution of the migrating speed of alternate bars during their occurrence and development by employing the proposed formula of the migrating speed. We provided a function for calculating the formula in Fortran. Please refer to the details of this function at Ishihara and Yasuda (2022).

4.2.1 Spatial distribution of the migrating speed of alternate bars

We used the proposed formula, Eq. (19) and Eq. (20), to obtain the results of the spatial distribution of the migrating speed of alternate bars. The calculated results are shown at the bottom of the three figures in Figure 8. The figure shows the dimensionless migrating speed, where the migrating speed is divided by the velocity of the uniform flow at initial. M is the migrating speed obtained from the proposed formula, and u_0 is the velocity of the uniform flow. The hatched area in the figure shows that the Shields number is less than the critical Shields number, and the migrating speed in the area is given in a forcing 0.

An almost flat bed 1 min from beginning of the experiments in Figure 8 (a), M/u_0 has almost no spatial distribution. The bed surface uniformly migrated at a speed of approximately 0.0015 at this time. After the bed was slightly changed from 10 min to 40 min, as shown in Figure 8 (b) to (e), M/u_0 began to show spatial distribution. Subsequently, the spatial distribution of M/u_0 was significantly changed from 60 min to 110 min, as shown in Figure 8 (g) to (l). The spatial distribution of M/u_0 increased at the deposited area and the front edge of the bars, and it decreased in the other areas.

Figure 10 shows a histogram of the magnitude of the spatial distribution of M/u_0 at each time. The red and blue vertical lines in the figure show the mean and the mean \pm the standard deviation of M/u_0 at each time, and each value is shown at the top of the figure. The shape of the histogram 1 min from the beginning of the experiment was concentrated around an average value of 0.00143, as shown in Figure 10(a). At this time, the standard deviation was 0.00015, and the spatial distribution of M/u_0 was little. When alternate bars occurred from 10 min to 60 min, the shape of the histogram became flat, the mean value of M/u_0 was 0.00126, and the standard deviation was 0.00023, as shown in Figure 10(b) to (g). From 1 min to 60 min, the mean value decreased by approximately 12 %, and the standard deviation increased to nearly 1.5 times. This change shows that the spatial distribution of the migrating speed greatly expanded from the flat bed to the occurrence of alternate bars. As shown in Figure 10(g) to (l), from 60 min to 110 min, the shape of the histogram changed from a sharp shape to a flat shape, and the standard deviation increased. Moreover, there was a significant decrease in the mean value of M/u_0 . The mean value of M/u_0 of (l) is 0.78 times that of 1 min, as shown in Figure 10(a), and the standard deviation of 110 min is 2.4 times that of 1 min.

Overall, we found that the migrating speed of alternate bars has spatial distribution, which expands from the occurrence stage to the development stage of alternate bars.

4.2.2 Magnitude of the migrating speed of alternate bars

We discussed the magnitude of the migrating speed of alternate bars and showed that the migrating speed has spatial distribution, which gradually expands, as shown in Figure 10. Their migrating speeds were divided by the velocity of the uniform flow on the flat bed at the initial time of the experiment. The velocity of the uniform flow was 0.28 m/s. The magnitude of the migrating speed was in the order of 10^{-4} to 10^{-3} of the velocity of the uniform flow at any location, regardless of the developmental state of the bars. We inferred that the deformation velocity of the bed surface is sufficiently smaller than the flowing velocity.

5 Discussion

We discussed the dominant physical quantity of the migrating speed and its approximate description in 5.1. Moreover, we discussed the decreasing factor of the migrating speed of alternate bars in 5.2. We also showed that the migrating speeds obtained using the proposed formula agree with those obtained from the instability analysis in 5.3.

5.1 Main dominant physical quantity and an approximate description of the migrating speed

The migrating speed of free bars could be quantified by both measurements and the proposed formula in this study. Moreover, the validity of the calculated migrating speed was confirmed. In this section, the dominant physical quantity of the migrating speed is discussed based on the mathematical structure of the formula.

Figure 11 (a) shows relationships between the energy slope, the Shields number, and the dimensionless migrating speed at the final time of the flume experiment. This figure indicates that the dimensionless migrating speed is proportional to the Shields number and energy slope. Because the dimensionless migrating speed is a product of the Shields number and energy slope, it is difficult to say which is dominant. At least, in this experiment, the energy slope is closer to the order of the dimensionless migrating speed, indicating that the energy slope is the more dominant physical quantity.

Thus, it can be inferred that the energy slope can describe the approximate migrating speed. Whether this approximate description is possible was examined based on the relationship between M/u_0 and $0.4 \times I_e$, as shown in Figure 11 (b). The correlation coefficients between the two at each time are shown in the figure. The value of 0.4 multiplied by the formula is a coefficient determined from the particle size, which is one of the variables in the denominator of formulas (19) and (20).

The relationship between M/u_0 and $0.4 \times I_e$ shows that the relationship is almost linear at all times, and the correlation coefficients are above 0.9 on average, indicating that the two have a strong positive correlation. These results suggest that the energy slope can approximately describe the migrating speed of alternate bars.

5.2 Decreasing factor for the migrating speed of alternate bars

In this subsection, the decreasing factor for the migrating speed of alternate bars is discussed. Figure 12 shows the average longitudinal distributions of the (a)

512 migrating speed, (b) energy line, hydraulic headline, and bed line over time. We
 513 conducted the laboratory flume experiment without sediment feed in §2. As shown
 514 in Figure 12(b), the slope of the bed level and each hydraulic head in the upstream
 515 section gradually became more gradual with the progress of time. The water level
 516 and energy head in the upstream section also decreased from the initial stage, and
 517 the water surface slope and energy slope, including the slope of the bed level, be-
 518 came more gradual. The flowing depth did not change much from the initial value
 519 in the whole section. It can also be seen that Figure 12 (a) the migrating speed in
 520 the same section decreased from the initial value. In contrast, at 5.5 m from the
 521 upstream end, the flowing depth hardly changed from the initial value, the energy
 522 slope increased, and the migrating speed increased.

523 We suggest that the dominant physical quantities of the migrating speed are
 524 the energy slope, grain size, and Shields number, as mentioned in the previous sec-
 525 tion. We estimated the decreasing factors of the migrating speed of alternate bars in
 526 this experiment based on these dominant physical quantities as follows. The grain
 527 size would not change the migrating speed because a single grain size was used in
 528 the experiment. The flowing depth would not change the migrating speed because
 529 the measured flowing depth was constant. In contrast, the energy slope significantly
 530 decreased. This decrease in the energy slope was due to the decrease in the bed
 531 level, which was because there was no-sediment supply at the upstream end. These
 532 results indicate that the reason for the decrease in the migrating speed of the alter-
 533 nate bars in this experiment is the decrease in the energy slope due to the decrease
 534 in the bed slope.

535 Eekhout et al. (2013) observed the occurrence and development processes of
 536 alternate bars in an actual river. He reported that the migrating speed of bars de-
 537 creased when the bed slope decreased. Their results imply that the decrease in the
 538 migrating speed is not based on the flowing depth and grain size, as their observa-
 539 tion was conducted in the same section and with the same flood magnitude. We as-
 540 sumed that the reason for the decrease in the migrating speed was the decrease in
 541 energy slope associated with the decrease in the bed slope, as in our experiment.

542 **5.3 Comparison between the migrating speed of our method and** 543 **that of instability analyses**

544 The conditions for the occurrence of free alternate bars were determined by in-
 545 stability analyses for bed perturbations given as initial conditions (Callander, 1969;
 546 Kuroki & Kishi, 1984). In these analyses, the migrating speed of the bed pertur-
 547 bations was calculated using the formulas below. These formulas were proposed by
 548 Bertagni et al. (2018). Eq. (28) was obtained from a linear analysis, and Eq. (29)
 549 was obtained from a weakly nonlinear analysis as shown below.

$$550 \quad M_{*(L.)} = -\frac{\text{Im}[\Omega]}{k} \quad (28)$$

$$M_{*(W.N.L.)} = -\left(\frac{\text{Im}[\Omega] - \text{Im}[\Xi] \frac{\text{Im}[\Omega]}{\text{Re}[\Xi]}}{k}\right) \quad (29)$$

551 where $M_{*(L.)}$ is the nondimensional migrating speed from the linear instability anal-
 552 ysis, $M_{*(W.N.L.)}$ is the nondimensional migrating speed from the weakly nonlinear
 553 instability analysis, Ω is the amplification factor, k is the wavenumber, and Ξ is the
 554 Landau Coefficient. For details on how to calculate the amplification factor Ω and
 555 Landau Coefficient Ξ , please refer to the original publication (Bertagni et al., 2018).

556 Their form of the formula and the derivation process of the formula are quite
 557 different from the proposed formula in this study. However, both formulas have simi-

lar physical properties and can be used to calculate similar migrating speeds. In this section, we compared the migrating speed obtained from the proposed formula in this study with the migrating speed obtained from instability analyses.

Figure 13 shows the relationship between the migrating speed obtained from the proposed formula in this study and the migrating speed obtained from instability analyses. The migrating speed obtained from instability analyses was also obtained from the formulas proposed by Bertagni et al. (2018). The vertical axis of the figure is the migrating speed of the proposed formula, which is shown as a box-and-whisker diagram for three time periods: 1 min at the initial bed, 50 min at the time of bar occurrence, and 120 min at the final time under each hydraulic condition shown in Table 1. The horizontal axis of the figure is the migrating speed of the instability analyses, and it shows the obtained results of the linear and weakly nonlinear analyses when the same hydraulic conditions in Table 1 were used.

(a) to (c) in Figure 13 show the migrating speed of the alternate bars from the occurrence stage to the development stage. The horizontal axis of (a) to (c) in Figure 13 shows that the migrating speed of the instability analysis and that the migrating speed of the weakly nonlinear instability analysis is slower than that of the linear instability analysis. The linear migrating speed is that of the dominant wavenumber at the time of occurrence of the alternate bars, and the weakly nonlinear migrating speed is that of the same dominant wavenumber when the wave height increased. The vertical axis of (a) to (c) in Figure 13 also shows that the migrating speed of the authors decreased on average from the occurrence stage to the development stage of the alternate bars. We found that similar trends with regard to the migrating speed from the occurrence stage to the development stage of alternate bars can be obtained from both our formulas and the instability analyses.

6 Applicability of the formula to rivers

In §4, we confirmed that the formula for calculating the migrating speed, which was derived in §3, has sufficient applicability to the flume experiment conducted in §2. Moreover, we determined the dominant quantity of the migrating speed, as shown in §5. In §6, We also show the applicability of the formula to an actual river, in which the scale, bed material, and hydraulic conditions were completely different from those in the flume experiment in §2.

6.1 Flood summary for a target river

We performed the following calculations for Chikuma River. Chikuma River is part of Shinano River, which is the longest river in Japan, with a channel length of about 300 km. Chikuma River is located in the upper basin of Shinano River and flows through Nagano Prefecture, as shown in Figure 14(a). Owing to the flood caused by Typhoon No. 19 in October 2019, the water level was close to the bank top for approximately 10 hours (Figure 15(b)). Figure 15(a) shows the discharge observed at the Ikuta observed station in Figure 14(b), where the maximum discharge during the flood reached over 7,200 m³/s. This is the largest discharge ever recorded and the 8th highest water level ever recorded in the history of observation.

Figure 1(a), (b) shows aerial photographs of the river channel before and after the flood in Ueda City (shown in Figure 14(b)). Figure 1 shows that alternate bars widely migrated downstream after the flood. The sky blue line and the blue line in Figure 1 (b) show the stream at low flow rates before and after the flood, respectively. Since the planar arrangement of the stream depends on the planar arrangement of the bars, the migrating distance of the stream during flooding was probably the migrating distance of the bars before and after flooding. The bars seem to have

607 migrated 450–800 m in the downstream direction during this flood, and this migra-
 608 tion would be due to the flood of October 2019.

609 **6.2 Hydraulic analysis for evaluating the migrating speed**

610 To obtain the migrating speed using the proposed formula, we performed one-
 611 dimensional unsteady flow calculations for a general crosssection. The governing
 612 equations used in this calculation are shown below. The reason for the one-dimensional
 613 analysis is that it is difficult to obtain detailed information for hydraulic calculations
 614 in actual rivers.

$$\frac{\partial A}{\partial t} + \frac{\partial Q}{\partial x} = 0 \quad (30)$$

615

$$\frac{\partial Q}{\partial t} + \frac{\partial}{\partial x} \left(\frac{Q^2}{A} \right) + gA \frac{\partial}{\partial x} (z + h) + \frac{gn^2 Q |Q|}{R^{4/3} A^2} = 0 \quad (31)$$

616 where A is the flow area, Q is the flow discharge, t is the time, x is the distance, z is
 617 the bed level, h is the flowing depth, n is Manning’s roughness coefficient, and R is
 618 the hydraulic mean depth.

619 We performed the calculation from the 84-km point at the Kuiseke observation
 620 station to the 109.5-km point at the Ikuta observation station, as shown in Figure
 621 14(b). The calculations used survey data of cross sections taken at 500-m intervals,
 622 measured in 2017 before the flood. We confirmed that from 2017 to 2019, there were
 623 no floods that would significantly change the channel geometry. The river bed mate-
 624 rial was given by varying it as a linear function in the computational section because
 625 it was 20 mm at the downstream end and 70 mm at the upstream end of the com-
 626 putational section. The roughness coefficient was given by the Manning–Strickler
 627 equation. The upstream boundary condition is the flow discharge at the Ikuta obser-
 628 vation station, as shown in Figure 15(a), and the downstream boundary condition is
 629 the water level at the Kuiseke observation station, as shown in Figure 15(b).

630 Eq. (32) is a one-dimensionalized expression, and it was obtained by finding
 631 the composite component of equations (19) and (20). The migrating speeds at each
 632 section were obtained by substituting the hydraulic quantities obtained above in Eq.
 633 (32).

$$M = \frac{4(\tau_* - \tau_{*c})^{1/2} \sqrt{sgd^3} I_e}{sd(1 - \lambda)} \left[1 - \frac{\gamma'}{\tau_*^{1/2}} \left\{ 1 - \frac{1}{3\tau_*} (\tau_* - \tau_{*c}) \right\} \frac{\partial z}{\partial x} \right] \quad (32)$$

634 **6.3 Comparison of the theoretical and field migrating speeds**

635 Figure 16 shows the longitudinal distribution of the calculated and measured
 636 migrating speeds, and Figure 16 only shows the section of the calculation in Figure
 637 1. The green line in the figure shows the calculation results at each flow discharge
 638 marked in Figure 15, from 1,000 m³/s, when sediments began moving throughout
 639 the section, to 7,200 m³/s, the peak flow discharge. The gray symbols in the figure
 640 show the measured migrating speed, implying an average migrating speed during the
 641 flood period. The average migrating speeds were calculated from the relationship
 642 between the migrating time and migrating distance of the stream at the low flow
 643 rate, assuming that an active sediment transport continued for approximately 29
 644 hours based on the hydrograph of Figure 15.

645 The calculation results of the migrating speed at each flow discharge show that
 646 the migrating speed had spatial distribution at each flow discharge and that it in-

647 creased with the increase in the flow discharge. The spatial distributions of the cal-
648 culated migrating speeds were generally similar, with the exception of the 104-km
649 point, although the magnitude of the calculated values was about half that of the
650 measured values. These results suggest that the migrating speed depends on the
651 spatial distribution of hydraulic quantities.

652 7 Conclusion

653 In this study, we discovered the existence of a migrating speed for free alter-
654 nate bars, quantified the magnitude of the migrating speed and its spatial distri-
655 bution, and further identified the dominant quantity for the migrating speed. The
656 main results obtained from this study are as follows.

- 657 1) We conducted a flume experiment with continuously flowing water and showed
658 the existence of migrating speeds based on measurements of bed level defor-
659 mations.
- 660 2) To quantify the spatial distribution of the migrating speed of alternate bars
661 using the coefficient (advection velocity) of the advection term in an HPDE,
662 we assumed that the bottom surface is a continuous function and derived an
663 HPDE for bed levels.
- 664 3) To verify the derived HPDE, we showed that it adequately describes the tem-
665 poral variation in the bed level.
- 666 4) We found that the proposed formula of the migrating speed of alternate bars
667 can calculate the spatial distributions of migrating speeds in flume experi-
668 ments. We also showed that its spatial distribution is temporally varying.
- 669 5) We showed that the magnitude of the migrating speed of alternate bars is ap-
670 proximately 10^{-3} to 10^{-4} orders of magnitude less than the velocity of the
671 uniform flow at flat beds before the occurrence of alternate bars.
- 672 6) We suggested that the dominant physical quantities of the migrating speed
673 are the energy slope, grain size, and Shields number. We also showed that the
674 reason for the decrease in the migrating speed of alternate bars is the decrease
675 in the energy slope due to the decrease in the bed slope.
- 676 7) We showed that the migrating speed obtained from the derived formula is in
677 agreement with that obtained from instability analyses.
- 678 8) We showed that the proposed formula is applicable to actual rivers, in which
679 the scale and hydraulic conditions differ from those in flume experiments.

680 Acknowledgments

681 The data used in this study can be accessed at Ishihara and Yasuda (2022). For
682 details of the data, please refer to the enclosed README.md. This work was sup-
683 ported by JSPS KAKENHI Grant Numbers JP21H04596, JP20K20543, and JICE
684 (No.19005 and No. 20004), Japan Institute of Country-ology and Engineering. We
685 performed the Mathematica code provided in the Supporting Information in Bertagni
686 et al.'s paper (Bertagni et al., 2018). The Ministry of Infrastructure, Land and Trans-
687 ports provided the measurement of the crosssection of Chikuma River. The essential
688 remarks made by associate editor and the reviewers helped us to refine our article
689 significantly. We would like to express our gratitude to associate editor and the re-
690 viewers.

691 References

692 Adami, L., Bertoldi, W., & Zolezzi, G. (2016). Multidecadal dynamics of alternate
693 bars in the alpine rhine river. *Water Resour. Res.*, *52*(11), 8938–8955. doi:

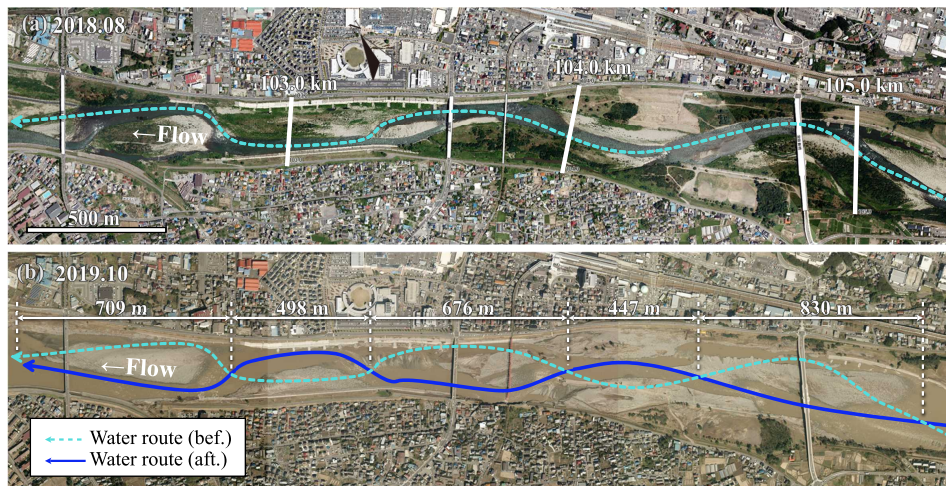


Figure 1. Aerial photos of the Chikuma river of Japan (a) before the flood, (b) after the flood (「Part 2 Chikumagawa teibou chousa iinnkai shiryō」 (Ministry of Land, Infrastructure, Transport and Tourism) (<https://www.hrr.mlit.go.jp/river/chikumagawateibouchousa/chikuma-02.pdf>) created by processing).

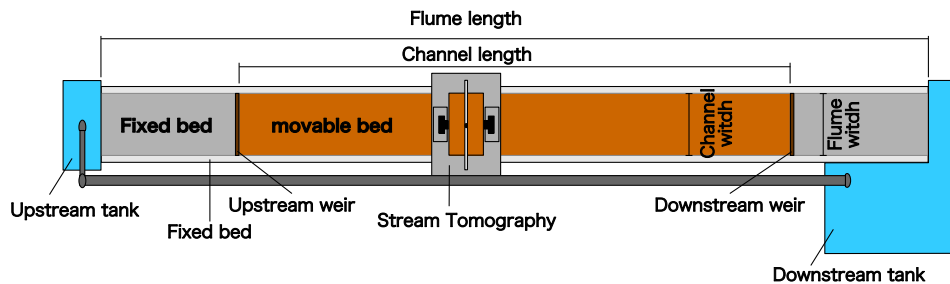


Figure 2. Plane view of the experimental flume.

- 694 <https://doi.org/10.1002/2015WR018228>
 695 Bertagni, M. B., Perona, P., & Camporeale, C. (2018). Parametric transitions be-
 696 tween bare and vegetated states in water-driven patterns. *Proc. Natl. Acad.*
 697 *Sci. U.S.A.*, *115*(32), 8125–8130. doi: 10.1073/pnas.1721765115
 698 Callander, R. A. (1969). Instability and river channels. *J. Fluid Mech.*, *36*(3), 465–
 699 480. doi: 10.1017/S0022112069001765
 700 Colombini, M., Seminara, G., & Tubino, M. (1987). Finite-amplitude alternate bars.
 701 *J. Fluid Mech.*, *181*, 213–232. doi: 10.1017/S0022112087002064
 702 Colombini, M., & Tubino, M. (1991). Finite-amplitude free bars: A fully nonlinear
 703 spectral solution. *Sand Transport in Rivers, Estuaries and the Sea*, 163–169.
 704 Crosato, A., Desta, F. B., Cornelisse, J., Schuurman, F., & Uijttewaal, W. S. J.
 705 (2012). Experimental and numerical findings on the long-term evolution of
 706 migrating alternate bars in alluvial channels. *Water Resour. Res.*, *48*(6). doi:
 707 10.1029/2011WR011320
 708 Crosato, A., Mosselman, E., Beidmariam Desta, F., & Uijttewaal, W. S. J. (2011).
 709 Experimental and numerical evidence for intrinsic nonmigrating bars in allu-
 710 vial channels. *Water Resour. Res.*, *47*(3). doi: 10.1029/2010WR009714
 711 Eekhout, J. P. C., Hoitink, A. J. F., & Mosselman, E. (2013). Field experiment on
 712 alternate bar development in a straight sand-bed stream. *Water Resour. Res.*,
 713 *49*(12), 8357–8369. doi: 10.1002/2013WR014259

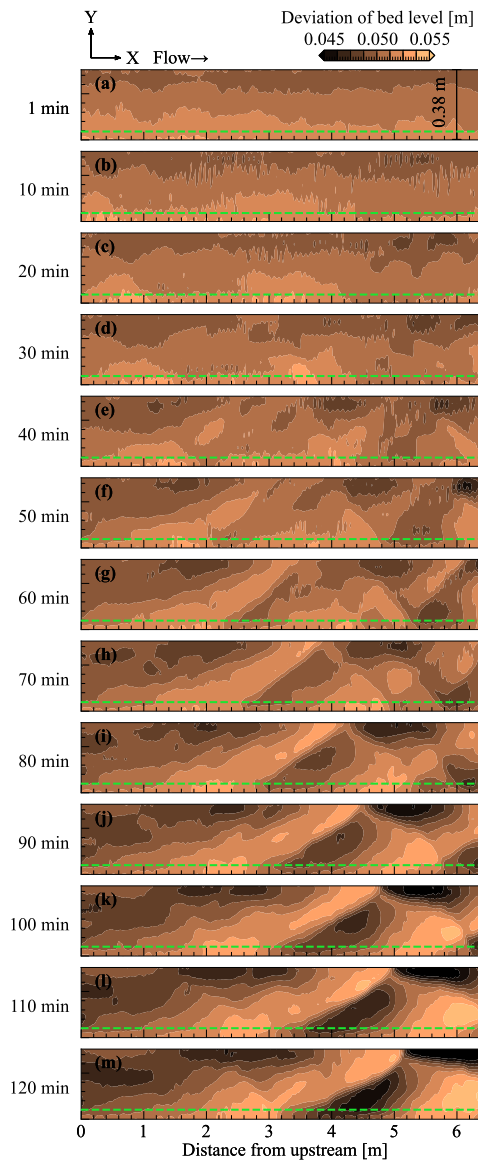


Figure 3. Temporal changes of the plane view in the observed bed topography.

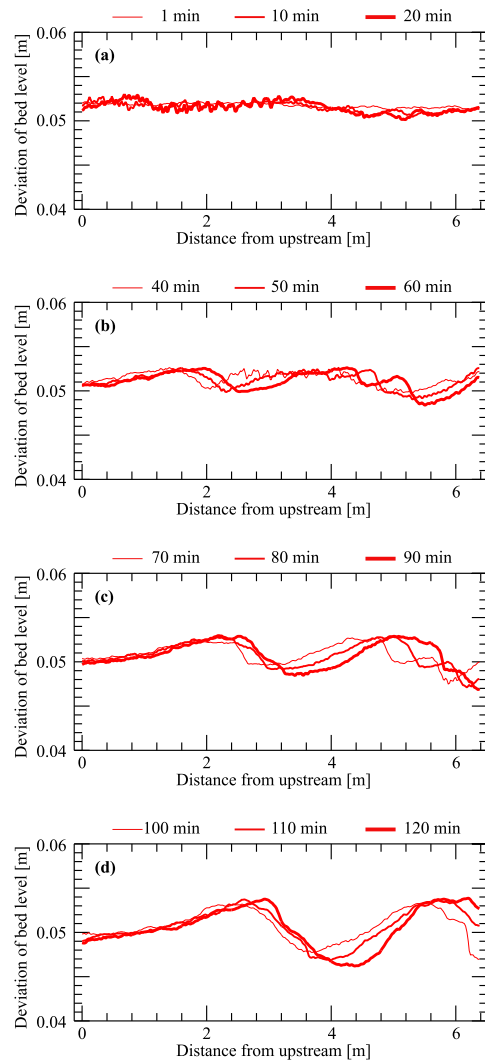


Figure 4. Longitudinal view of the measured bed shape: (a) Initial stage of the experiment, (b) occurrence of alternate bars, (c) intermediate stage of the experiment, and (d) final stage of the experiment.

- 714 Federici, B., & Seminara, G. (2003). On the convective nature of bar instability. *J.*
 715 *Fluid Mech.*, *487*, 125–145. doi: 10.1017/S0022112003004737
 716 Fujita, Y., Koike, T., Furukawa, R., & Muramoto, Y. (1985). Experiments on the
 717 initial stage of alternate bar formation. *Disaster Prevention Research Institute*
 718 *Annals (in Japanese)*, *28*(B-2), 379–398.
 719 Fujita, Y., & Muramoto, Y. (1982). Experimental study on stream channel processes
 720 in alluvial rivers. *Bulletin of the Disaster Prevention Research Institute*, *32*(1),
 721 49–96.
 722 Fujita, Y., & Muramoto, Y. (1985). Studies on the process of development of al-
 723 ternate bars. *Bulletin of the Disaster Prevention Research Institute*, *30*(3),
 724 55–86.
 725 Hayashi, T., Ozaki, Y., & Onishi, K. (1982). On the mechanism of occurrence of
 726 three-dimensional bed configurations. *Proceedings of the Japan Society of Civil*

- 727 *Engineers (in Japanese)*, 26, 17–24. doi: 10.2208/prohe1975.26.17
- 728 Ikeda, H. (1983). Experiments on bedload transport, bed forms, and sedimentary
729 structures using fine gravel in the 4-meter-wide flume..
- 730 Ishihara, M., & Yasuda, H. (2022). *Dataset*. (<https://doi.org/10.4121/16788778.v1>)
- 731 Iwagaki, Y. (1956). Hydrodynamical study on critical tractive force. *Transactions*
732 *of the Japan Society of Civil Engineers (in Japanese)*, 41, 1–21. doi: 10.2208/
733 jscej1949.1956.41_1
- 734 Izumi, N., & Pornprommin, A. (2002). Weakly nonlinear analysis of bars with the
735 use of the amplitude expansion method. *Journal of JSCE (in Japanese)*, 712,
736 73–86. doi: 10.2208/jscej.2002.712.73
- 737 Kennedy, J. F. (1963). The mechanics of dunes and antidunes in erodible-bed chan-
738 nels. *J. Fluid Mech.*, 16(4), 521–544. doi: 10.1017/S0022112063000975
- 739 Kinoshita, R. (1958). Experiment on dune length in straight channel. *Journal of*
740 *the Japan Society of Erosion Control Engineering (in Japanese)*, 30, 1–8. doi:
741 10.11475/sabo1948.1958.30_1
- 742 Kinoshita, R. (1961). Investigation of channel deformation in ishikari river. *Rep.*
743 *Bureau of Resources, Dept. Science & Technology, Japan. (in Japanese)*.
- 744 Kuroki, M., & Kishi, T. (1984). Regime criteria on bars and braids in alluvial
745 straight channels. *Proceedings of the Japan Society of Civil Engineers (in*
746 *Japanese)*, 342, 87–96. doi: 10.2208/jscej1969.1984.342_87
- 747 Lanzoni, S. (2000a). Experiments on bar formation in a straight flume: 1. uni-
748 form sediment. *Water Resour. Res.*, 36(11), 3337–3349. doi: 10.1029/
749 2000WR900160
- 750 Lanzoni, S. (2000b). Experiments on bar formation in a straight flume: 2.
751 graded sediment. *Water Resour. Res.*, 36(11), 3351–3363. doi: 10.1029/
752 2000WR900161
- 753 Miwa, H., Daido, A., & Katayama, T. (2007). Effects of water and sediment dis-
754 charge conditions on variation in alternate bar morphology. *Proceedings of hy-*
755 *draulic engineering (in Japanese)*, 51, 1051–1056. doi: 10.2208/prohe.51.1051
- 756 Moteki, D., Murai, T., Hoshino, T., Yasuda, H., Muramatsu, S., & Hayasaka, K.
757 (2022). Capture method for digital twin of formation processes of sand bars.
758 *Phys. Fluids*, 34(3), 034117. doi: 10.1063/5.0085574
- 759 Nagata, N., Muramoto, Y., Uchikura, Y., Hosoda, T., Yabe, M., Takada, Y., &
760 Iwata, M. (1999). On the behaviour of alternate bars under several kinds of
761 channel conditions. *Proceedings of Hydraulic Engineering (in Japanese)*, 43,
762 743–748.
- 763 Nelson, P., & Morgan, J. (2018, 09). Flume experiments on flow and sediment
764 supply controls on gravel bedform dynamics. *Geomorphology*, 323. doi:
765 10.1016/j.geomorph.2018.09.011
- 766 Ozaki, S., & Hayashi, T. (1983). On the formation of alternating bars and braids
767 and the dominant meander length. *Proceedings of the Japan Society of Civil*
768 *Engineers (in Japanese)*, 1983(333), 109–118. doi: 10.2208/jscej1969.1983.333
769 _109
- 770 Podolak, C. J. P., & Wilcock, P. R. (2013). Experimental study of the response of
771 a gravel streambed to increased sediment supply. *Earth Surf Process Landf*,
772 38(14), 1748–1764. doi: 10.1002/esp.3468
- 773 Schielen, R., Doelman, A., & Swart, H. E. (1993). On the nonlinear dynamics of free
774 bars in straight channels. *J. Fluid Mech.*, 252, 325–356.
- 775 Seminara, G. (2010). Fluvial sedimentary patterns. *Annu. Rev. Fluid Mech.*, 42(1),
776 43–66. doi: 10.1146/annurev-fluid-121108-145612
- 777 Shimizu, Y., & Itakura, T. (1989). Calculation of bed variation in alluvial channels.
778 *J. Hydraul. Eng.*, 115(3), 367–384. doi: 10.1061/(ASCE)0733-9429(1989)115:
779 3(367)
- 780 Shimizu, Y., Nelson, J., Ferrel, K. A., Asahi, K., Giri, S., Inoue, T., ... Yamaguchi,
781 S. (2019). Advances in computational morphodynamics using the international

- 782 river interface cooperative (iric) software. *Earth Surf Process Landf*, 45(1),
 783 11–37. doi: 10.1002/esp.4653
- 784 Tubino, M. (1991). Growth of alternate bars in unsteady flow. *Water Resour. Res.*,
 785 27(1), 37–52. doi: 10.1029/90WR01699
- 786 Venditti, J. G., Nelson, P. A., Minear, J. T., Wooster, J., & Dietrich, W. E. (2012).
 787 Alternate bar response to sediment supply termination. *J. Geophys. Res.*
 788 *Earth. Surf.*, 117(F2). doi: 10.1029/2011JF002254
- 789 Watanabe, A., Fukuoka, S., Yasutake, Y., & Kawaguhi, H. (2001). Groin arrange-
 790 ments made of natural willows for reducing bed deformation in a curved chan-
 791 nel. *Advances in river engineering (in Japanese)*, 7.

792 Appendix A Validity of the Pseudo-steady Flow Assumption Ap- 793 plied to Bars-Scale Riverbed Waves

794 We describe the validity of the pseudo-steady flow assumption applied to the
 795 bar-scale riverbed waves. In this study, we introduced the assumption of a pseudo-
 796 steady flow when deriving the HPDE for bed level z . This assumption is often intro-
 797 duced in instability analyses of bar-scale riverbed waves (Callander, 1969; Kuroki &
 798 Kishi, 1984). In the above instability analysis, we assumed that the migrating speed
 799 of the bed is sufficiently slower than the migrating speed of the flow, and the flow
 800 can be treated as a pseudo-steady flow if the flow rate is constant. Based on this
 801 assumption, for instability analysis, we ignore the term of the time gradient in the
 802 continuity equation of flow and the equation of motion of flow among the governing
 803 equations that are used in the analysis. The above assumptions would be reasonable
 804 because the previous instability analysis explains the occurrence and developmen-
 805 tal mechanisms of alternate bars. On the other hand, this assumption is probably
 806 unproven. Therefore, we verified whether the term of the flow time gradient can be
 807 ignored with ST measurement values and hydraulic analysis.

808 The verification was performed by comparing the magnitude of each term in
 809 the equation of motion for flow.

$$\frac{1}{g} \frac{\partial u}{\partial t} + \frac{u}{g} \frac{\partial u}{\partial x} + \frac{\partial H}{\partial x} + I_{ex} = 0 \quad (\text{A1})$$

810 where H is the water level. The magnitude of each term in the equation was calcu-
 811 lated for each measurement time of ST, and the magnitudes were compared.

812 $\partial H/\partial x$ was obtained with the measured value of the water level of the ST.
 813 Other terms were obtained with the results of the hydraulic analysis, which is de-
 814 scribed in §4. The time interval and spatial interval of the calculation were 1 min
 815 and 2 cm, respectively, which are the time resolutions and spatial resolutions of ST.
 816 The flow velocity and migrating speed of the y component under the experimental
 817 conditions were 10^{-4} to 10^1 of the x components at any location regardless of the
 818 developmental state of the alternate bars. For simplicity, the y component is ignored
 819 in this section.

820 Figure A1 shows the time change of the box-beard diagram that displays the
 821 magnitude of each term. This Figure shows the (a) local term, (b) advection term,
 822 (c) pressure term, and (d) friction term, which correspond to the order of each term
 823 in Eq. (A1). The figure shows that although the (b) advection term, (c) pressure
 824 term, and (d) friction term dominate the flow at any time, it can be confirmed that
 825 (a) the local term can be ignored because it is smaller than the three terms. Even
 826 if the advection term with the smallest magnitude in (b), (c), and (d) is compared
 827 with the local term, the magnitude of the local term is 10^{-4} to 10^{-2} of the (b) ad-

vection term, the local term is extremely small. From this, it is inferred that it is physically appropriate to ignore the time gradient of flow in the alternate bars.

Appendix B Derivation of the Two-Dimensional Equation of the Water Surface Profile

We show the derivation processes of the two-dimensional equation of the water surface profile to derive the HPDE for the bed level. The governing equations used for the derivation consist of the following continuous equations and the equations of motion. When deriving the equation, the flow can be treated as a pseudo-steady-state flow based on the verification results in Appendix A. Therefore, the following continuous equations and equations of motion were used for the derivation.

$$\frac{\partial[hu]}{\partial x} + \frac{\partial[hv]}{\partial y} = 0 \quad (\text{B1})$$

$$\frac{u}{g} \frac{\partial u}{\partial x} + \frac{v}{g} \frac{\partial u}{\partial y} + \frac{\partial z}{\partial x} + \frac{\partial h}{\partial x} + I_{ex} = 0 \quad (\text{B2})$$

$$\frac{u}{g} \frac{\partial v}{\partial x} + \frac{v}{g} \frac{\partial v}{\partial y} + \frac{\partial z}{\partial y} + \frac{\partial h}{\partial y} + I_{ey} = 0 \quad (\text{B3})$$

As explanation of the various physical quantities has already been provided, it is omitted here.

The derivation of $\partial h/\partial x$ is described as follows. First, applying the product rule to Eq. (B1) results in the following equation.

$$h \frac{\partial u}{\partial x} + u \frac{\partial h}{\partial x} + h \frac{\partial v}{\partial y} + v \frac{\partial h}{\partial y} = 0 \quad (\text{B4})$$

For the first and third terms on the left side of Eq. (B4),

$$u = \frac{1}{n} \frac{I_{ex}}{I_e^{1/2}} h^{2/3} \quad (\text{B5})$$

$$v = \frac{1}{n} \frac{I_{ey}}{I_e^{1/2}} h^{2/3} \quad (\text{B6})$$

$$\frac{\partial u}{\partial x} = \frac{\partial u}{\partial h} \frac{\partial h}{\partial x} + \frac{\partial u}{\partial I_{ex}} \frac{\partial I_{ex}}{\partial x} + \frac{\partial u}{\partial I_e} \frac{\partial I_e}{\partial x} = \frac{2}{3} \frac{u}{h} \frac{\partial h}{\partial x} + \frac{u}{I_{ex}} \frac{\partial I_{ex}}{\partial x} - \frac{1}{2} \frac{u}{I_e} \frac{\partial I_e}{\partial x} \quad (\text{B7})$$

$$\frac{\partial v}{\partial y} = \frac{\partial v}{\partial h} \frac{\partial h}{\partial y} + \frac{\partial v}{\partial I_{ey}} \frac{\partial I_{ey}}{\partial y} + \frac{\partial v}{\partial I_e} \frac{\partial I_e}{\partial y} = \frac{2}{3} \frac{v}{h} \frac{\partial h}{\partial y} + \frac{v}{I_{ey}} \frac{\partial I_{ey}}{\partial y} - \frac{1}{2} \frac{v}{I_e} \frac{\partial I_e}{\partial y} \quad (\text{B8})$$

After differentiating the composite function (Eq. (B7) and Eq. (B8)) using Manning's formula (Eq. (B5), Eq. (B6)), substituting it into Eq. (B4), and rearranging $\partial h/\partial x$, the following equation is obtained.

$$\frac{\partial h}{\partial x} = -\frac{3}{5} \frac{h}{I_{ex}} \frac{\partial I_{ex}}{\partial x} + \frac{3}{10} \frac{h}{I_e} \frac{\partial I_e}{\partial x} - \frac{v}{u} \frac{\partial h}{\partial y} - \frac{3}{5} \frac{vh}{u I_{ey}} \frac{\partial I_{ey}}{\partial y} + \frac{3}{10} \frac{vh}{u I_e} \frac{\partial I_e}{\partial y} \quad (\text{B9})$$

After substituting Eq. (B7) and the following Eq. (B10) into the first and second terms of the equation of motion in the x direction for Eq. (B2), we get

$$\frac{\partial u}{\partial y} = \frac{\partial u}{\partial h} \frac{\partial h}{\partial y} + \frac{\partial u}{\partial I_{ex}} \frac{\partial I_{ex}}{\partial y} + \frac{\partial u}{\partial I_e} \frac{\partial I_e}{\partial y} = \frac{2}{3} \frac{u}{h} \frac{\partial h}{\partial y} + \frac{u}{I_{ex}} \frac{\partial I_{ex}}{\partial y} - \frac{1}{2} \frac{u}{I_e} \frac{\partial I_e}{\partial y} \quad (\text{B10})$$

853 Eq. (B9), which was organized earlier into Eq. (B11), we get

$$\begin{aligned} & \frac{2 u^2}{3 g h} \frac{\partial h}{\partial x} + \frac{u^2}{g I_{e x}} \frac{\partial I_{e x}}{\partial x} - \frac{1 u^2}{2 g I_e} \frac{\partial I_e}{\partial x} + \frac{2 u v}{3 g h} \frac{\partial h}{\partial y} \\ & + \frac{u v}{g I_{e x}} \frac{\partial I_{e x}}{\partial y} - \frac{1 u v}{2 g I_e} \frac{\partial I_e}{\partial y} + \frac{\partial z}{\partial x} + \frac{\partial h}{\partial x} + I_{e x} = 0 \end{aligned} \quad (\text{B11})$$

854 The following equation can be obtained by rearranging $v/u\partial h/\partial y$.

$$\begin{aligned} & \frac{v}{u} \frac{\partial h}{\partial y} = \frac{3}{5 I_{e x}} \left(\frac{u^2}{g} - h \right) \frac{\partial I_{e x}}{\partial x} + \frac{3}{10 I_e} \left(-\frac{u^2}{g} + h \right) \frac{\partial I_e}{\partial x} \\ & + \frac{1}{5 I_{e y}} \left(-\frac{2 u v}{g} - \frac{3 v h}{u} \right) \frac{\partial I_{e y}}{\partial y} + \frac{3}{10 I_e} \left(-\frac{u v}{g} + \frac{v h}{u} \right) \frac{\partial I_e}{\partial y} + \frac{u v}{g I_{e x}} \frac{\partial I_{e x}}{\partial y} + \frac{\partial z}{\partial x} + I_{e x} \end{aligned} \quad (\text{B12})$$

855 After substituting Eq. (B12) into Eq. (B9) and rearranging it, the following $\partial h/\partial x$
856 is derived.

$$\frac{\partial h}{\partial x} = -\frac{\partial z}{\partial x} - I_{e x} - \frac{3 u^2}{5 g I_{e x}} \frac{\partial I_{e x}}{\partial x} + \frac{3 u^2}{10 g I_e} \frac{\partial I_e}{\partial x} + \frac{2 u v}{5 g I_{e y}} \frac{\partial I_{e y}}{\partial y} + \frac{3 u v}{10 g I_e} \frac{\partial I_e}{\partial y} - \frac{u v}{g I_{e x}} \frac{\partial I_{e x}}{\partial y} \quad (\text{B13})$$

857 By rearranging $\partial h/\partial y$ using the same process as before, the following equation for
858 $\partial h/\partial y$ is obtained.

$$\frac{\partial h}{\partial y} = -\frac{\partial z}{\partial y} - I_{e y} - \frac{3 v^2}{5 g I_{e y}} \frac{\partial I_{e y}}{\partial y} + \frac{3 v^2}{10 g I_e} \frac{\partial I_e}{\partial y} + \frac{2 u v}{5 g I_{e x}} \frac{\partial I_{e x}}{\partial x} + \frac{3 u v}{10 g I_e} \frac{\partial I_e}{\partial x} - \frac{u v}{g I_{e y}} \frac{\partial I_{e y}}{\partial x} \quad (\text{B14})$$

859

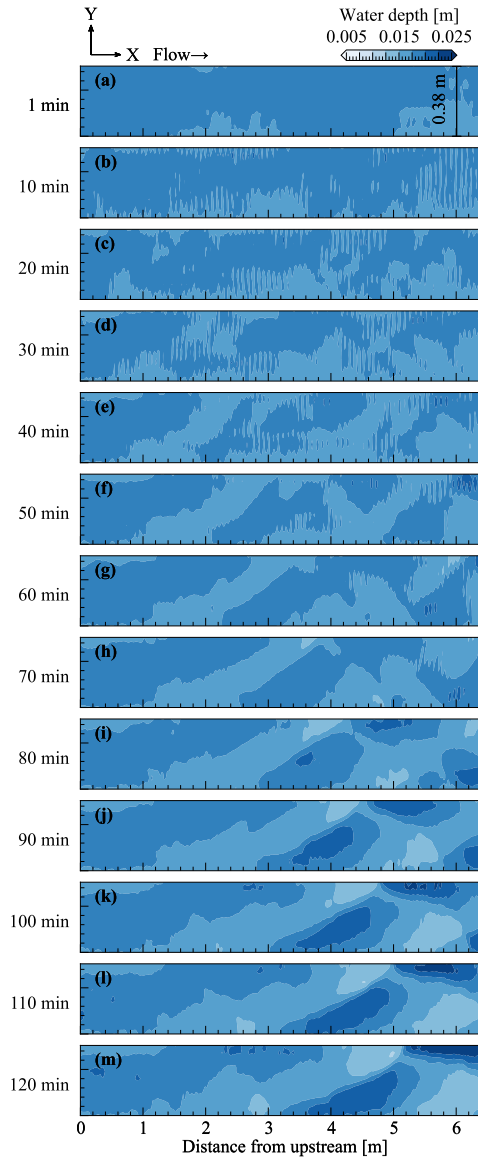


Figure 5. Temporal changes in the plane view for the observed water depth.

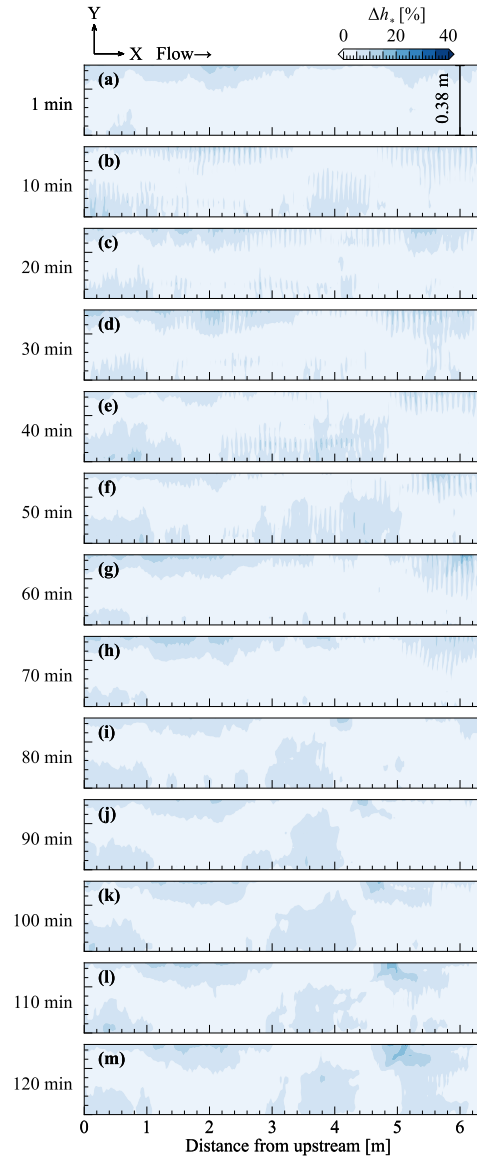


Figure 6. Difference between the measured and calculated values of the water depth that is made dimensionless using the measured value.

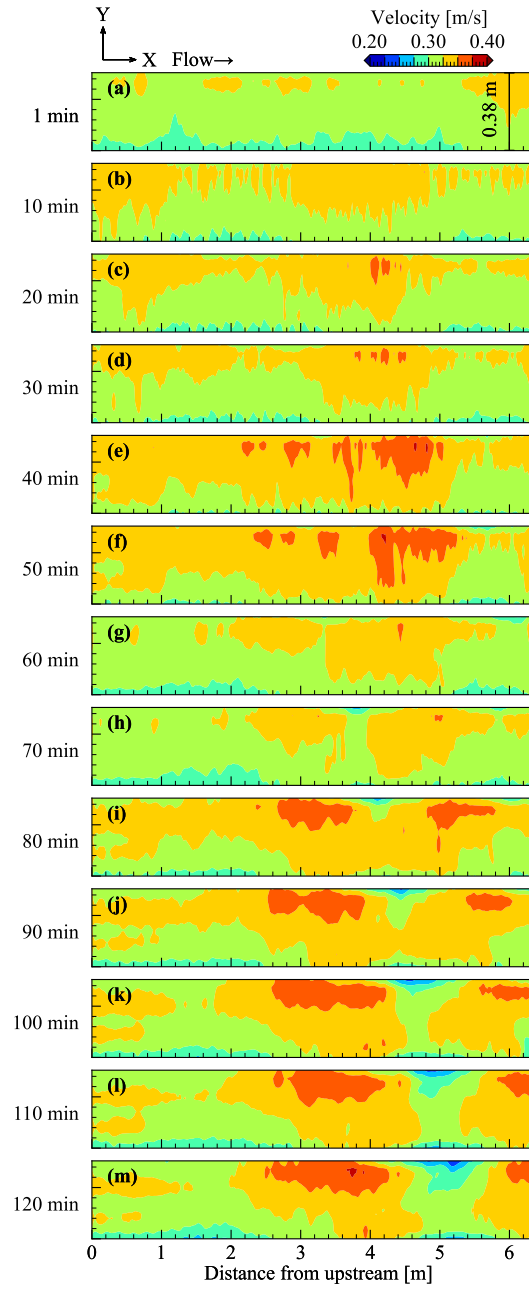


Figure 7. Temporal changes in the plane view for the calculated flow velocity.

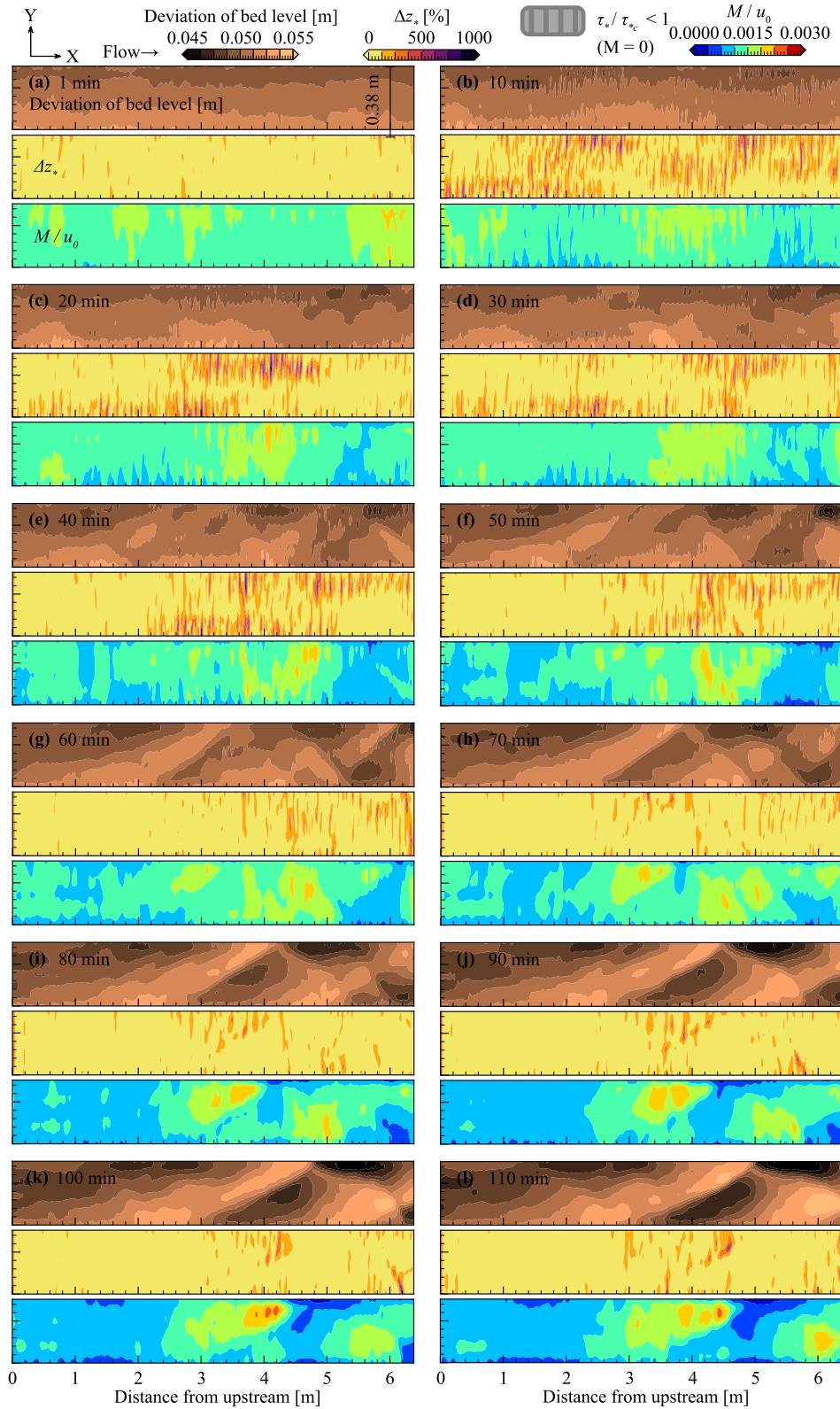


Figure 8. Temporal changes of the plane view in the observed bed topography, Δz_* and calculated migrating speed.

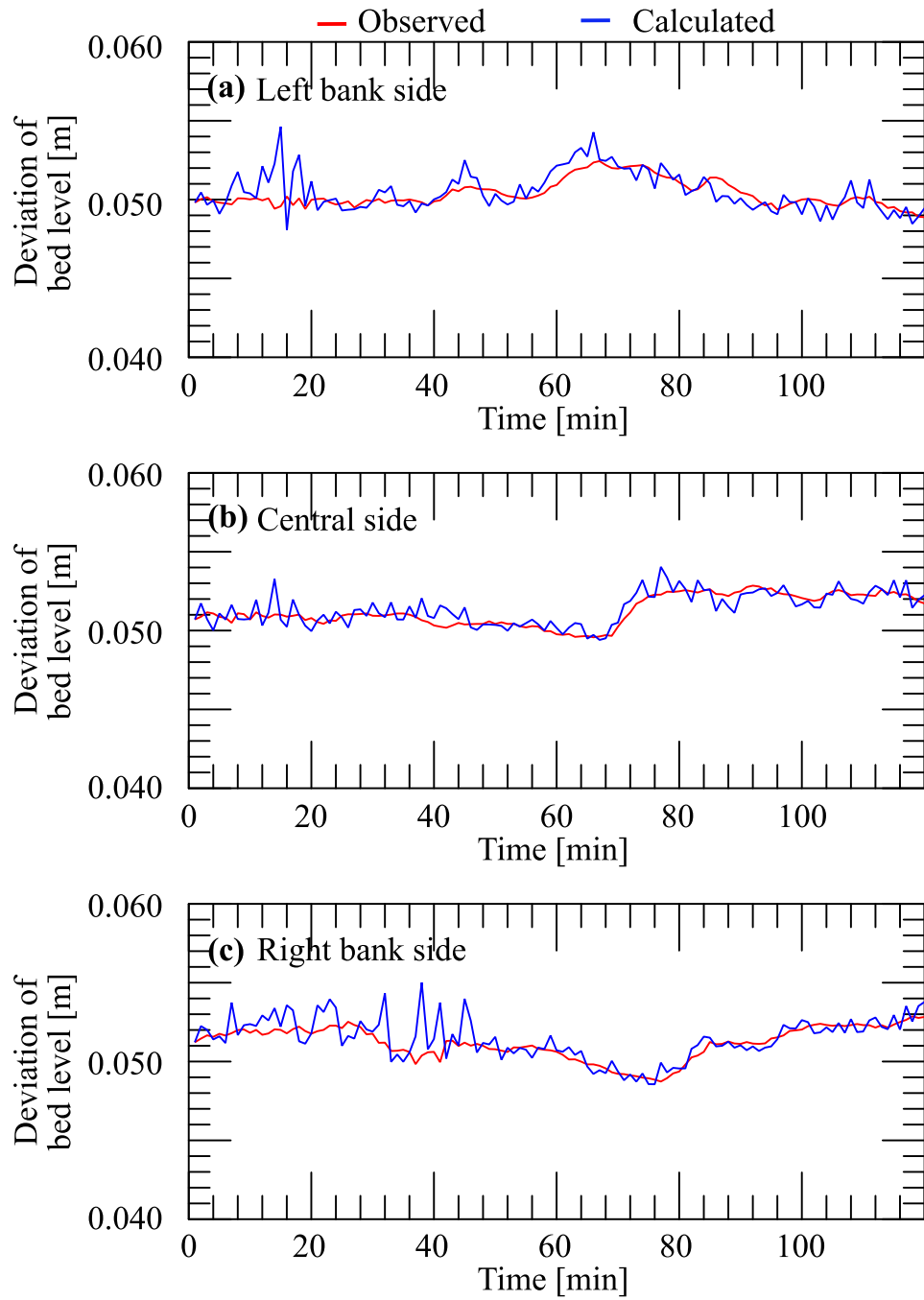


Figure 9. Bed-level temporal waveform: (a) Left bank side, (b) center, (c) right bank side.

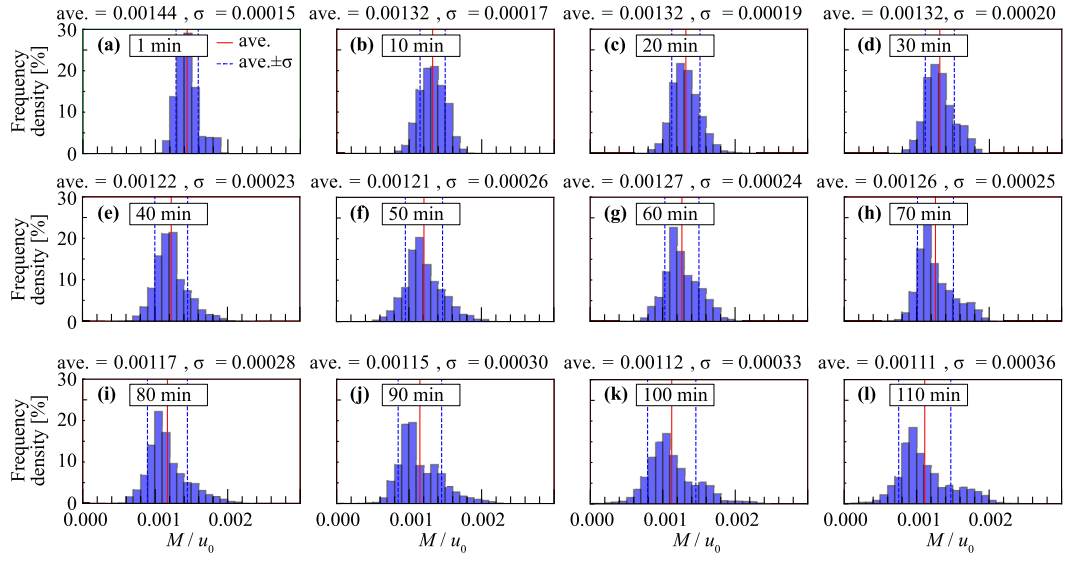


Figure 10. Histograms of migrating speed.

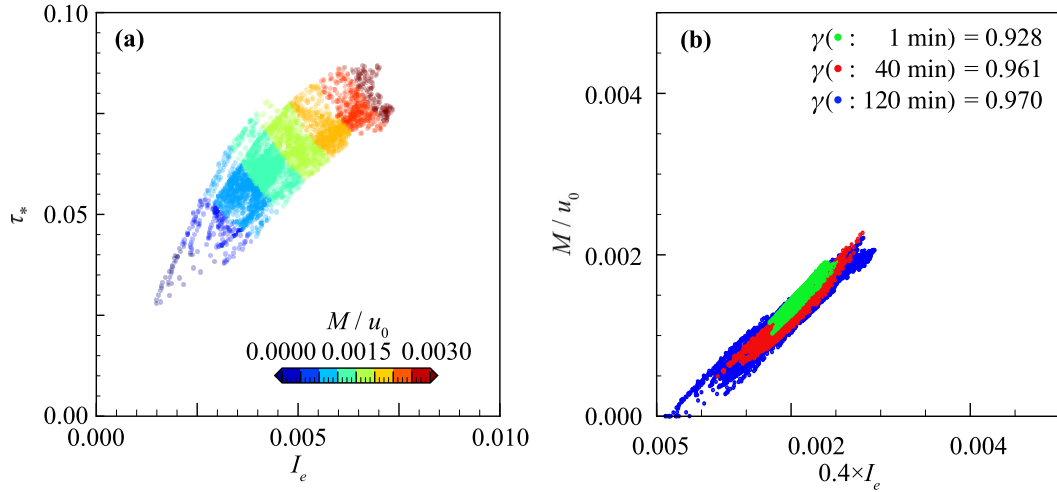


Figure 11. (a) Relationship between energy slope, Shields number, and migrating speed, (b) Relationship between migrating speed and energy slope.

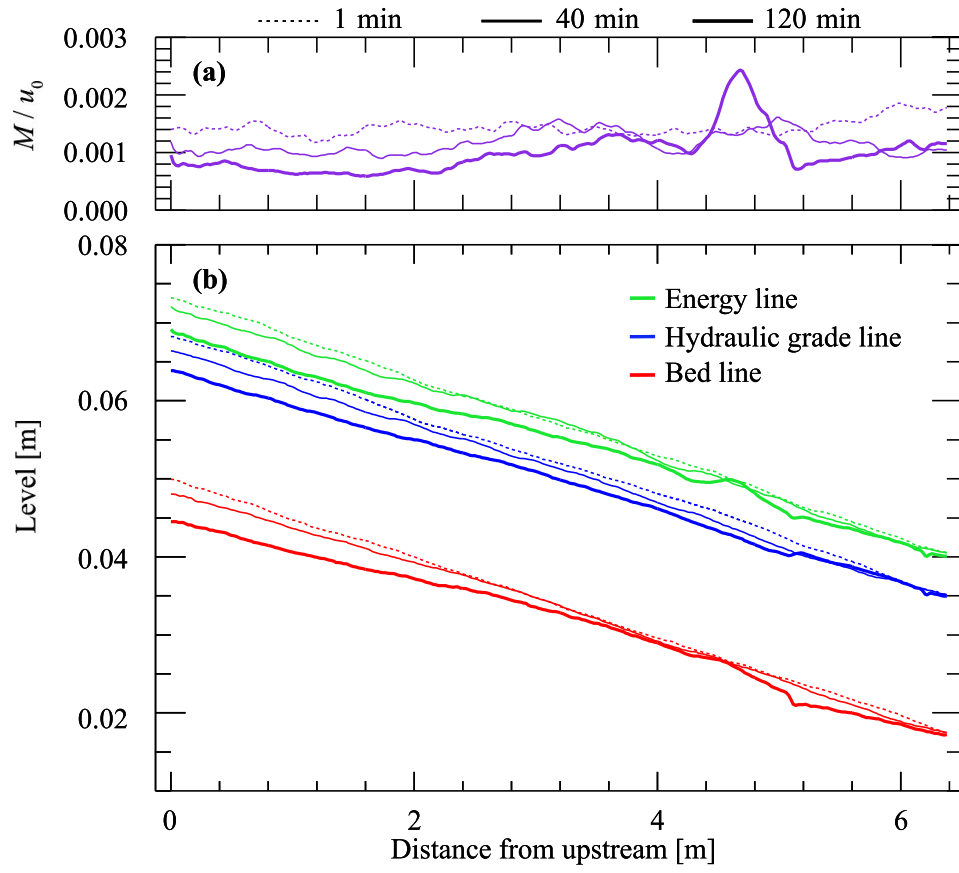


Figure 12. Longitudinal view of the (a) cross-sectional averaged migrating speed (b) and cross-sectional averaged bed level.

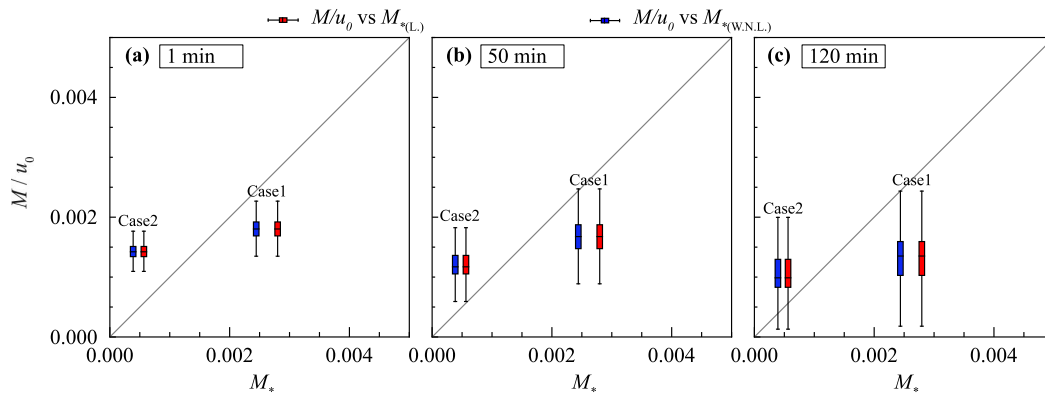


Figure 13. Relationship between migrating speed obtained by our method and migrating speed obtained by instability analysis.

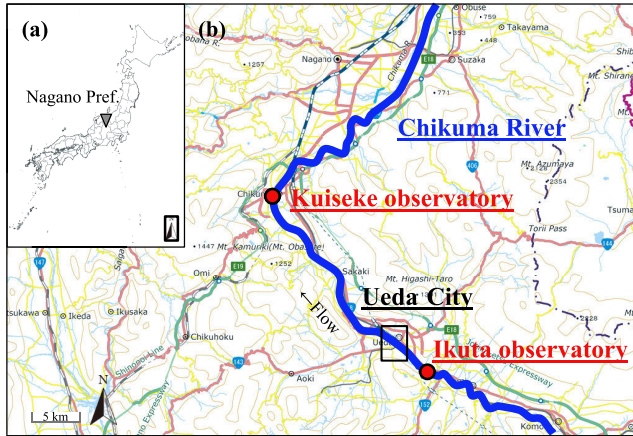


Figure 14. Overview of the study area: (a) geographic location, (b) map (GSI Maps (electronic land web) created by processing).

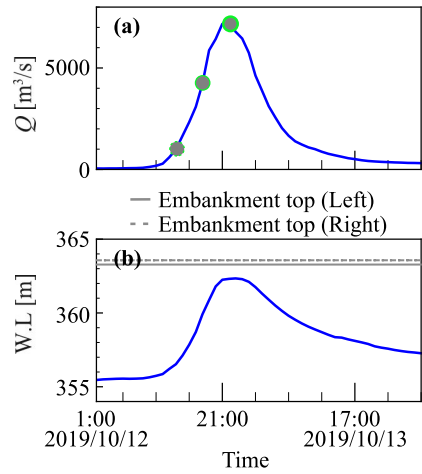


Figure 15. (a) Flow discharge hydrograph and (b) water level hydrograph.

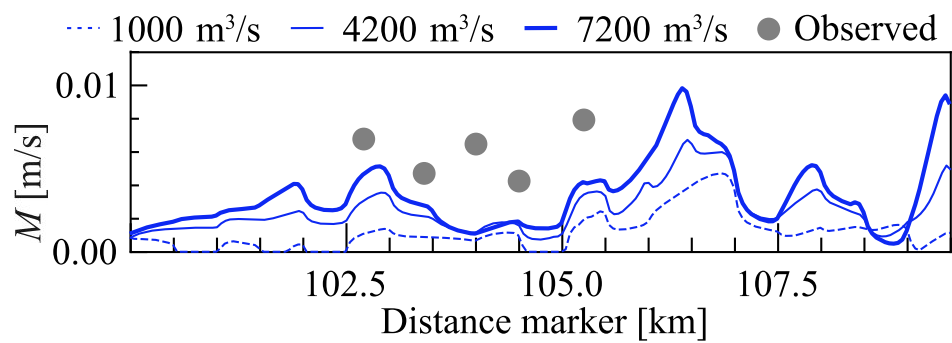


Figure 16. Calculated and measured values of migrating speed.

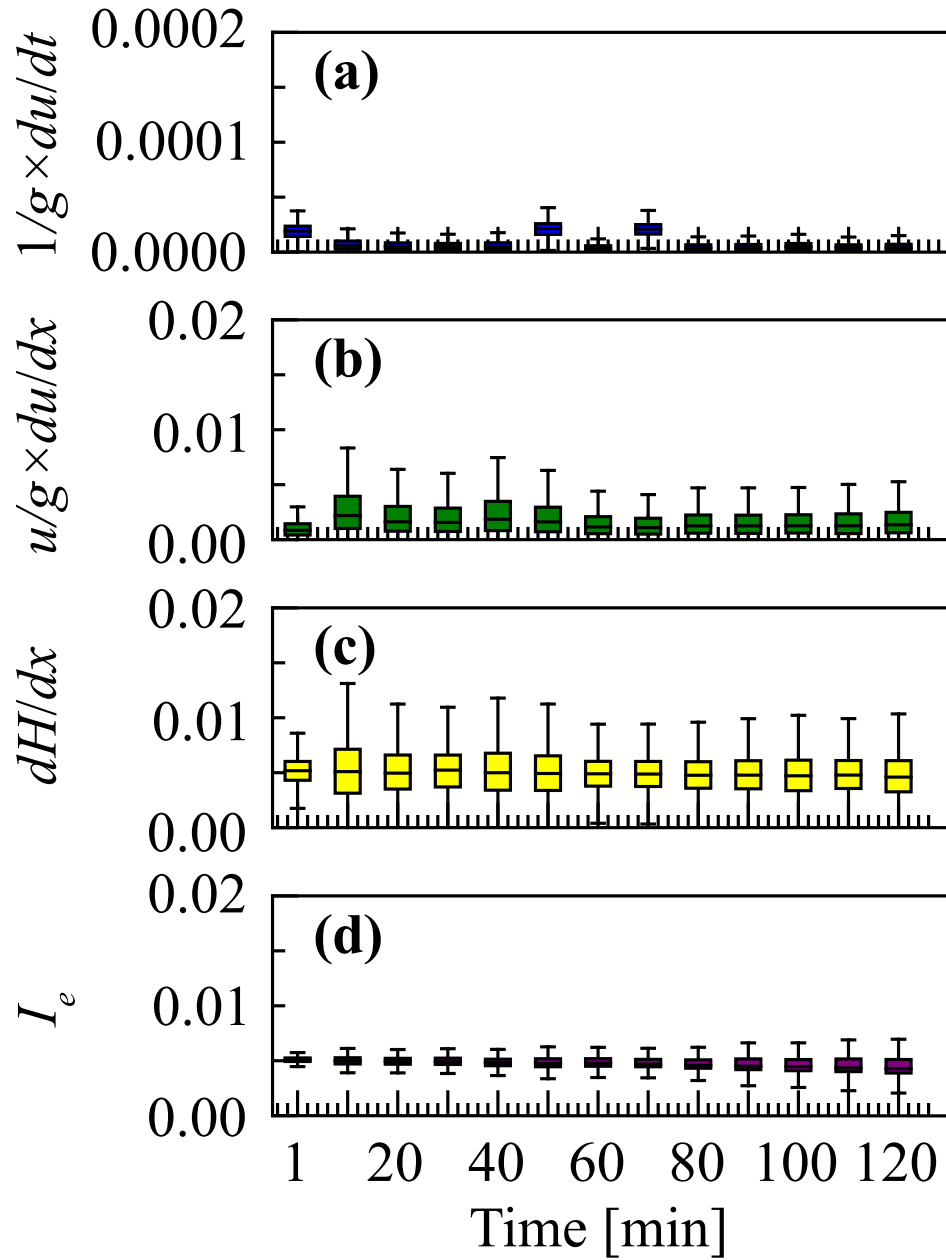


Figure A1. Temporal changes of the box plots for the (a) local term, (b) advection term, (c) pressure term, and (d) friction term.